Intrinsic instabilities in premixed hydrogen flames

Intrinsic Instabilities in Premixed Hydrogen Flames: Parametric Variation of Pressure, Equivalence Ratio, and Temperature. Part 2 - Non-Linear Regime and Flame Speed Enhancement

Lukas Berger[a,*], Antonio Attili[b], Heinz Pitsch[a]

[a]*Institute for Combustion Technology, RWTH Aachen University, 52056 Aachen, Germany*
[b]*Institute for Multiscale Thermofluids, School of Engineering, University of Edinburgh, Edinburgh, EH9 3FD, United Kingdom*

Abstract

The propensity of lean premixed hydrogen flames to develop intrinsic instabilities is studied by means of a series of simulations at different equivalence ratios [0.4-1.0], unburned temperatures [298K-700K], and pressures [1bar-20bar]. In addition to the Darrieus-Landau or hydrodynamic instability, lean premixed hydrogen flames are prone to thermodiffusive instabilities, which lead to significant flame front wrinkling and a chaotic process of formation and destruction of cellular structures along the flame front. In part 1 of this work (L.Berger et al., Combust. Flame, 2021), the stability of planar flames that are exposed to weak harmonic perturbations has been studied. In this part, the long-term dynamics of these flames, which become strongly corrugated and show strong flame speed enhancements and variations of the local reaction rates, are studied. In particular, local extinction events and strong peaks of the reaction rates, sub- and super-adiabatic temperatures in the burned gas, and variations of the local flame thickness are observed such that the flame reactivity significantly deviates from an unstretched laminar flamelet. Consistent with the stability analysis in part 1, the impact of instabilities increases if the equivalence ratio or unburned temperature are decreased or the pressure is increased. In particular, the propensity of intrinsic instabilities to increase at high pressure is relevant to several combustion applications operating at elevated pressures. Further, the effect of the global flame parameters such as the expansion ratio, Zeldovich number, and Lewis number on the flame speed enhancement is quantitatively assessed. Finally, the flame speed enhancement due to instabilities is found to correlate well with the maximum growth rates of the perturbed flames that have been measured in part 1 indicating a strong link between the two different flame regimes.

Keywords: Thermodiffusive Instability, DNS, Hydrogen, Premixed, Preferential Diffusion

1. Introduction

As discussed in part 1 of this study [1], lean hydrogen/air flames are prone to thermodiffusive combustion instabilities, which can substantially change flame dynamics, heat release rates, and flame speed. These combustion instabilities originate from the strong differential diffusion of hydrogen due to its low Lewis number, which leads to variations of the local equivalence ratio and hence reaction rates along the flame front. Additionally, the flame propagation is affected by the hydrodynamic instability mechanism, which arises from the density jump across the flame front, and exists for any premixed flame irrespective of the Lewis number.

In part 1 of this work, a stability analysis, in which planar flames are exposed to weak harmonic perturbations, was presented. Measuring the growth rates of the perturbations, the propensity of lean hydrogen flames to develop intrinsic instabilities was studied at different conditions by varying the equivalence ratio, the unburned temperature, and pressure. In part 1, only the very early evolution of the perturbed flames was studied, when the flame wrinkling that results from the initial perturbation remains small. In contrast, this part describes the long-term dynamics of these flames. For long times, significant flame wrinkling that induces high stretch rates along the flame front is observed and strong irregular flame front corrugations develop due to the intrinsic instabilities. To separate the two characteristic regimes, the initial phase will be termed 'linear' while the 'non-linear' phase refers to the long-term dynamics of these flames.

The long-term dynamics of lean premixed hydrogen flames have been analyzed in several numerical studies [2–11]. In all studies, the formation of small cellular structures that merge to larger cells and split again into smaller cells is observed along the flame front. For sufficiently large enough computational domain sizes, the dependence of the flame dynamics on the domain size becomes negligible and another characteristic large-scale corrugation of the flame front that is referred to as flame fingers was identified by Berger et al. [11]. These flame fingers propagate faster relative to the average flame front and interact with each other to form a strongly corrugated flame. Since the flame fingers tend to tilt sidewards with respect to the main flame propagation, they are eventually re-absorbed by the flame front and a periodic formation and destruction of such fingers

*Corresponding author
Email address: l.berger@itv.rwth-aachen.de (Lukas Berger)

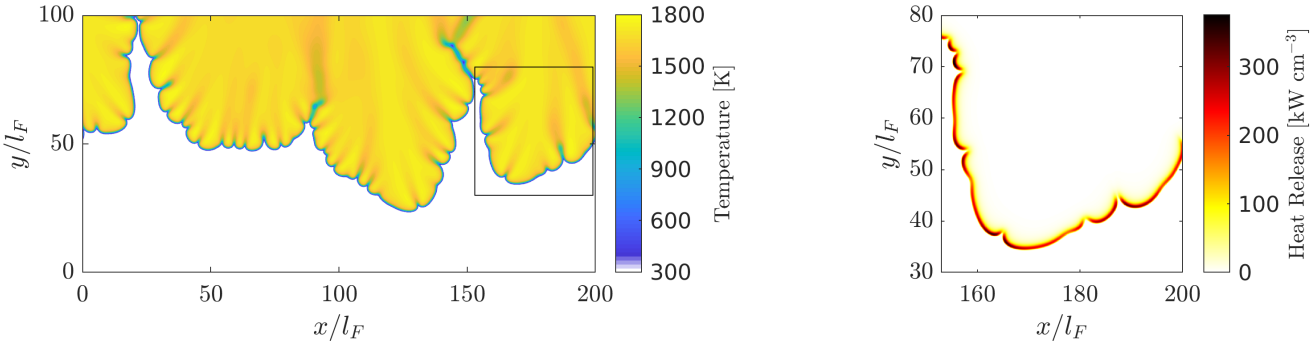

Figure 1: Case 'Ref': Snapshot of the temperature field showing small-scale cellular structures and large-scale finger-like structures along the flame front (left panel). Note that local temperatures strongly exceed the adiabatic temperature of T_b = 1643 K. The right panel shows a closeup of a flame finger colored with the heat release and the location of the closeup is indicated in the left panel by a rectangle.

is observed. The small-scale cellular structures and large-scale flame fingers are also seen in the studies of Fernández-Gallisteo et al. [10] and Yu et al. [9], who numerically studied lean hydrogen flames, and also in the experimental investigation by Wongwiwat et al. [12], who studied lean hydrogen flames in Hele-Shaw cells. The formation of flame fingers leads to a significant increase of flame surface area and affects the reactivity of the flame such that a significantly enhanced consumption speed, which can be several times larger than the laminar unstretched burning velocity, is observed. For instance, Berger et al. [11] observed a flame speed enhancement by a factor of four at an equivalence ratio of $\phi = 0.5$ at ambient conditions (T_u = 298 K, p = 1 bar).

To understand the origin of the characteristic small- and large-scale structures, it is essential to investigate the local flame state. For lean hydrogen/air flames, Bradely et al. [13] experimentally showed that the differential diffusion of hydrogen leads to a significant variation of the reactivity along the flame front leading to larger reaction rates in flame segments that are convexly curved towards the unburned gas and extinction pockets in the cusp regions. This results from the variation of the local equivalence ratio along the flame front due to the differential diffusion of hydrogen and has been similarly observed in numerical studies [14–17]. While this effect is well understood from a qualitative point of view, it is still necessary to quantitatively assess at which conditions (equivalence ratio, unburned temperature, and pressure) the effects of differential diffusion have a leading order effect or may be negligibly small. In particular, the fluctuations of the local equivalence ratio due to differential diffusion and the sensitivity of the reactivity on the local equivalence ratio need to be jointly assessed as both aspects directly impact the flame propagation. To systematically assess these aspects and provide a comprehensive picture of the effects of thermodiffusive instabilities for lean hydrogen/air flames for conditions of practical interest, a large parametric study of planar lean hydrogen/air flames is conducted for different values of the equivalence ratio, unburned temperature, and pressure. A series of high-fidelity simulations that employ a detailed chemical mechanism to avoid assumptions related to the reduction of chemical mechanisms and resolve all length and time scales, such as spatial gradients and the characteristic time scales of chemical reactions, has been performed to investigate the long-term dynamics of thermodiffusively unstable flames.

It is worth noting that this paper does not discuss the interactions of turbulence and the flame intrinsic instability mechanisms, as discussed for the hydrodynamic instability mechanism by Boughanem et al. [18] and Bychkov [19] and for lean premixed hydrogen/air flames by Aspden et al. [20], and the departure of the presented flame shapes from a planar flame front are solely caused by the flame intrinsic instability mechanisms.

In the following, the numerical configuration, the governing equations, and the conditions of the parametric variation are introduced. Thereafter, an analysis of the flame state, the enhancement of flame speeds, and the characteristic size of the cellular structures is performed. Finally, the paper discusses correlations based on power law fits that are validated against the numerical data and allow to predict the enhancement of flame speed for any value of equivalence ratio, unburned temperature, and pressure.

2. Configuration and Numerical Methods

2.1. Configuration

Several simulations of statistically planar, premixed, hydrogen/air flames at varying conditions have been conducted in a rectangular two-dimensional computational domain. A snapshot of the configuration is shown in Fig. 1, where the spatial distribution of temperature and heat release is shown. The rectangular domain is periodic in the crosswise direction denoted by x, while inflow and outflow boundary conditions are chosen for the streamwise direction denoted by y. For the inflow, a constant inlet velocity of the unburned mixture (entering at the bottom of the computational domain) is chosen such that the flame is stabilized within the domain. The value of the inlet velocity is determined by running each simulation at least twice, where the first run is performed with an estimated initial velocity and the observed consumption speed is then used to perform the final run, which can be run for a much longer time as the flame remains within the computational domain. In all cases, the flames are initialized as planar flame fronts that are perturbed by a small sinusoidal disturbance and propagate towards the inlet.

Table 1: Overview of the performed simulations. For each case, the equivalence ratio ϕ, the pressure p, the unburned temperature T_u, the laminar unstretched burning velocity s_L, the flame thickness l_F, the expansion ratio σ, the Zeldovich number β, the effective Lewis number Le_{eff}, the domain size $L_x \times L_y$, the computational grid $n_x \times n_y$, and the temporal discretization Δt are given. The asterisk for case 'Ref' indicates that the mesh is stretched in y-direction towards the inlet while all other cases are equidistant.

Case name	ϕ	p [bar]	T_u [K]	s_L [cm/s]	l_F [μm]	τ_F [ms]	σ	β	Le_{eff}	$L_x/l_F \times L_y/l_F$	$n_x \times n_y$	Δt [μs]
Reference case:												
Ref	0.5	1	298	45.2	438	0.97	5.04	9.2	0.37	$200 \times 150^*$	$3000 \times 1575^*$	1.0
Variation of equivalence ratio:												
Eq040	0.4	1	298	17.4	714	4.35	4.44	11.4	0.34	800×200	8192×2048	6.0
Eq065	0.65	1	298	99.8	363	0.36	5.79	7.4	0.43	200×200	2048×2048	1.0
Eq100	1.0	1	298	228.9	372	0.16	6.84	6.4	0.68	200×200	2048×2048	1.0
Variation of unburned temperature:												
Tu500	0.5	1	500	179.6	441	0.25	3.31	8.5	0.39	100×100	1024×1024	0.5
Tu700	0.5	1	700	523.2	533	0.10	2.57	3.8	0.44	100×100	1500×1500	0.5
Variation of pressure:												
p05	0.5	5	298	21.5	119	0.55	5.04	12.6	0.35	100×100	1500×1500	0.4
p10	0.5	10	298	12.0	92	0.76	5.04	16.5	0.34	100×100	1024×1024	0.3
Variation of pressure at T_u = 700K:												
Tu700p03	0.5	3	700	395.0	128	0.033	2.58	5.5	0.41	100×100	1500×1500	0.08
Tu700p10	0.5	10	700	216.8	33	0.015	2.58	7.5	0.38	100×100	1500×1500	0.02
Tu700p20	0.5	20	700	132.9	18	0.014	2.59	8.9	0.37	100×100	1500×1500	0.02

Tab. 1 summarizes all simulations that have been performed. As a reference case, the conditions of the unburned mixture are set to an equivalence ratio of $\phi = 0.5$, an unburned temperature $T_u = 298$K, and a pressure of $p = 1$bar. Parametric variations are conducted with respect to equivalence ratio, unburned temperature, and pressure while the other parameters are kept constant during this variation. In addition to these three variations, a fourth variation of pressure at $\phi = 0.5$ and $T_u = 700$K has been performed to include high pressure, high temperature conditions into the analysis that represent characteristic conditions for gas turbine applications [21]. A visualization of the four different parametric variations is shown in Fig. 2. Tab. 1 lists the burning velocity s_L and the thermal flame thickness l_F of a one-dimensional laminar unstretched flame, the flame's expansion ratio σ, the Zeldovich number β, and the effective Lewis number Le_{eff} of each case. The thermal flame thickness l_F is defined by the maximum gradient of temperature in a one-dimensional unstretched flame as

$$l_F = \frac{T_b - T_u}{\max(\nabla T)}, \tag{1}$$

where T_b is the adiabatic flame temperature, and the definitions of σ, β, and Le_{eff} are given in part 1 of this study [1]. Following Berger et al. [11], the domain size in the crosswise and streamwise directions, L_x and L_y, are chosen sufficiently large to obtain a value of the consumption speed, which is not affected by the domain size, and to not constrain the large-scale flame front corrugations labeled as flame fingers. A typical single finger structure can be observed in the closeup of Fig. 1. The negligible effect of the domain size on the consumption speed of thermodiffusively unstable planar flame fronts for sufficiently large

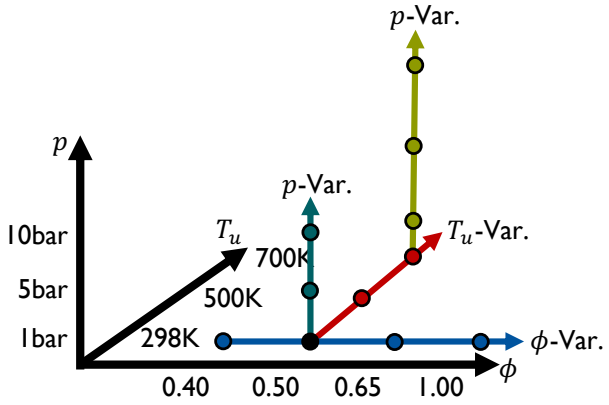

Figure 2: Visualization of the parametric variation of equivalence ratio, unburned temperature, and pressure.

domain sizes was also observed by Creta et al. [22], who compared findings among different groups. However, it is worth noting that for flames that are not affected by thermodiffusive instabilities but only by the hydrodynamic instability mechanism, a certain dependence on domain size can be observed, but Creta et al. [22] also concluded that the asymptotic behavior for large domain sizes is yet unclear for these cases.

Furthermore, it is worth noting that in comparison to the other cases, case 'Eq040' possesses a relatively large domain size L_x in lateral direction, which is much larger than the minimum required width to obtain a domain-independent flame speed, as it was designed for a previous analysis [11], in which the impact of the lateral domain size on the flame evolution was systematically studied.

2.2. Governing Equations and Numerical Methods

The flow is modeled by the reacting Navier-Stokes equations in the low-Mach limit [23] using detailed transport and the reaction mechanism of Burke et al. [24]. The same models and numerical methods as in part 1 of this work are applied and for further details the reader is referred to part 1 [1].

In contrast to part 1, where a very high mesh resolution and small timestep sizes were needed to study the linear phase while the amplitudes of the initial perturbations are very small, the mesh resolution and the timestep size of each simulation in this part can be larger and are chosen such that the laminar flame speed, heat release, temperature, and species profiles of a one-dimensional premixed unstretched flame computed by FlameMaster [25] are recovered adequately. For all cases, the laminar flame thickness is resolved by ten to fifteen grid points. The resulting meshes and timestep sizes are displayed in Tab. 1. All meshes are uniform in the x- and y-directions, with the exception of case 'Ref', which features an exponential mesh stretching with a stretch rate of 5% in the y-direction to enlarge the computational domain towards the inlet. The domain size in y-direction is $L_\mathrm{y} = 150 l_\mathrm{F}$ and the mesh stretching is only applied to the first third of the domain. Throughout the whole simulation, the flame stays in the unstretched part of the grid. The full domain size is shown in the movie in the supplementary material and is also displayed in Tab. 1, while Fig. 1 only includes the unstretched part of the mesh.

3. Results and Discussion

Intrinsic instabilities affect the flame dynamics of lean hydrogen flames and lead to a strong enhancement of the fuel consumption rate. As will be shown, this results from the effects of differential diffusion within the flame front. Thus, the local flame state and the effects of differential diffusion are described first. Thereafter, the analysis of the consumption speed and the effects of flame surface area are discussed.

3.1. Characteristic Pattern of Unstable Flames

For the description of the combustion process, two different progress variables are defined and discussed in the remainder of this paper. The first progress variable is defined by the mass fraction of water as

$$C_{\mathrm{H_2O}} = Y_{\mathrm{H_2O}} / Y_{\mathrm{H_2O,b}}, \tag{2}$$

where $Y_{\mathrm{H_2O,b}}$ refers to the value in the burned gas at adiabatic conditions. The second progress variable is based on the molecular hydrogen mass fraction yielding

$$C_{\mathrm{H_2}} = 1 - Y_{\mathrm{H_2}} / Y_{\mathrm{H_2,u}}, \tag{3}$$

where $Y_{\mathrm{H_2,u}}$ refers to the value in the unburned gas. The source term of each progress variable is given as

$$\dot{\omega}_{\mathrm{C_i}} = M_\mathrm{i} \dot{C}_\mathrm{i}, \tag{4}$$

where the index i refers to molecular hydrogen or water, M_i is the molar mass and $\dot{C}_\mathrm{i}$ refers to the change of concentration of molecular hydrogen or water due to chemical reactions. However, it is worth noting that both reaction rates $\dot{\omega}_{\mathrm{C_{H_2}}}$ and $\dot{\omega}_{\mathrm{C_{H_2O}}}$ are almost proportional to each other as shown in the supplementary material. Thus, for the analysis of the reaction rates, only $\dot{\omega}_{\mathrm{C_{H_2O}}}$ is studied in the following and, for simplicity, the index i of the reaction rates is omitted and $\dot{\omega}_\mathrm{C} = \dot{\omega}_{\mathrm{C_{H_2O}}}$.

Fig. 3 shows snapshots of the progress variable $C_{\mathrm{H_2O}}$ during the non-linear evolution of the different cases. Note that for the sake of comparability, only a part of the simulation domain of $100 l_\mathrm{F} \times 100 l_\mathrm{F}$ is shown for each case. After the initialization, the flame undergoes a transition in which the imposed periodicity of the initial perturbation is still visible and, eventually, a chaotic non-linear flame propagation is observed. Movies of all cases are provided in the supplementary material. For several cases, the formation of finger-like large-scale structures is seen while additional small cells are formed along the flame front. It is worth noting the overshoots of $C_{\mathrm{H_2O}}$ that prevail in post-flame regions, where the flame is convexly curved towards the unburned, in particular behind the flame-finger structures. Consequently, there exist also long trails of reduced values of $C_{\mathrm{H_2O}}$ behind the flame front that slowly mix with the super-unity values behind the flame front. As will be shown, these trails of sub- and super-unity values of $C_{\mathrm{H_2O}}$ result from local mixture fraction fluctuations along the flame front. Similar to the growth rates of the dispersion relations that were studied in part 1 of this work, the chaotic behavior of the flame propagation, the formation of small-scale cellular structures and flame fingers increase if the equivalence ratio or unburned temperature are decreased or if pressure is increased. Hence, a decrease of equivalence ratio or unburned temperature or an increase of pressure will be referred to as variations towards unstable conditions in the following. Conversely, towards stable conditions, the formation of flame fingers in Fig. 3 is diminished and the characteristic cusp at the tip of the flame fingers also vanishes as clearly evident for case 'Eq065'.

To highlight the impact of intrinsic instabilities on the flame evolution, Fig. 4 compares the strongly unstable case 'Ref' and the least unstable case 'Tu700'. The definition of stability is adopted from part 1 of this work [1], where numerical dispersion relations are measured and cases with high peak growth rates such as case 'Ref' are considered as strongly unstable while case 'Tu700' possesses the smallest peak growth rates compared to all cases. Fig. 4 shows a closeup of the spatial distribution of both progress variable definitions, the source term $\dot{\omega}_\mathrm{C}$, and the joint probability density function (PDF) of the source term $\dot{\omega}_\mathrm{C}$ and the progress variable $C_{\mathrm{H_2}}$. Comparing the two progress variables, sub- and super-unity values in the burned gas are only visible for $C_{\mathrm{H_2O}}$ in case 'Ref' while this is not possible for $C_{\mathrm{H_2}}$ as this would require negative values of $Y_{\mathrm{H_2}}$. The differential diffusion of hydrogen significantly affects the reactivity of the flame as can be seen from the spatial distribution of $\dot{\omega}_\mathrm{C}$, which has been normalized with the maximum value of an unstretched laminar flamelet. For the strongly unstable case 'Ref', significantly larger peak values compared to the corresponding unstretched flamelet and local extinction regions indicated by a vanishing heat release are visible while case 'Tu700' reveals an intact and uniform reaction

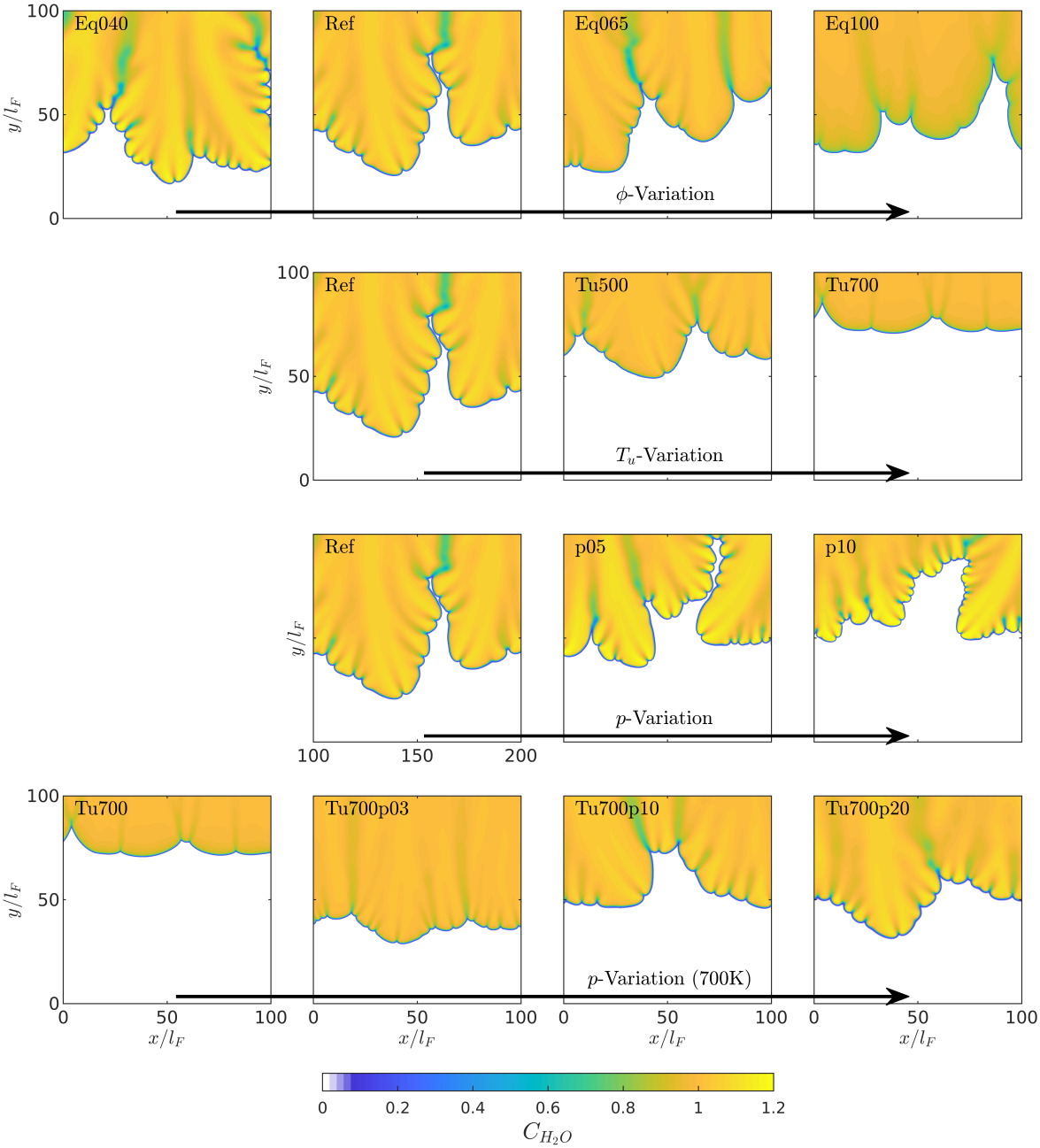

Figure 3: Snapshots of the spatial distribution of progress variable for all performed simulations. For the sake of comparability, only a part of the simulation domain of $100l_F \times 100l_F$ is shown and movies of the flame evolution in the full computational domain are provided in the supplementary material.

layer and $\dot{\omega}_C \approx \dot{\omega}_C^{\text{Flamelet}}$. The departure of the local reaction rates from the unstretched laminar flamelet in case 'Ref' becomes evident from the joint PDF of $\dot{\omega}_C$ and C_{H_2}, which shows a large scatter of $\dot{\omega}_C$. Also the conditional average (red curve) is significantly higher compared to the reaction rates of the unstretched flamelet (black curve). The reaction rates of case 'Tu700' closely follow the flamelet curve (the large probability values, the conditional mean and the flamelet overlap and are difficult to separate in Fig. 4). As will be shown, the reaction rate fluctuations result from local mixture fraction fluctuations and the same conclusions hold if looking at the joint PDF of C_{H_2O} and $\dot{\omega}_C$ as will be shown in Fig. 7.

3.2. *Analysis of Reaction Rate Fluctuations*

In the following section, details are provided to understand the root cause of the fluctuations of the reaction rates along the flame front and to find a suitable description of the flame state as the significant scatter of $\dot{\omega}_C$ with respect to C_{H_2} for case 'Ref' in Fig. 4 indicates that the progress variable is not sufficient to describe the local flame state and the progress variable source term. Therefore, to identify suitable quantities for

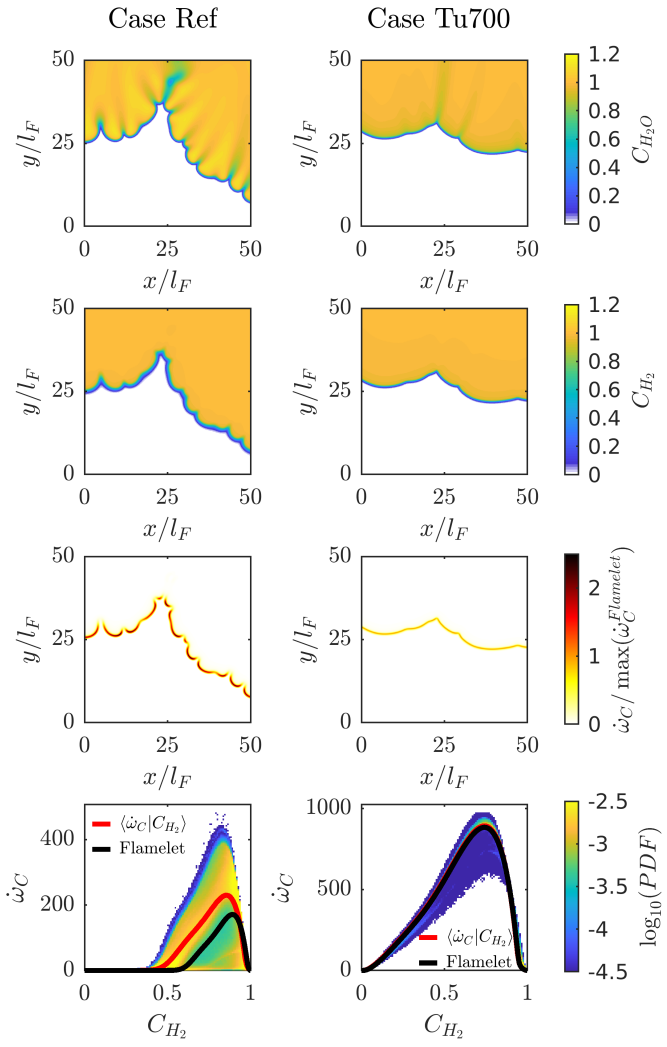

Figure 4: Comparison of cases 'Ref' and 'Tu700' (from top to bottom): Spatial distributions of both progress variables and the progress variable source term $\dot{\omega}_C$ and joint PDF of $\dot{\omega}_C$ and C_{H_2} that include the conditional mean (red curve) and the flamelet solution (black curve).

parametrizing $\dot{\omega}_C$, an optimal estimator analysis [26, 27] is conducted. In such an analysis, the capability of a set of parameters $\boldsymbol{\psi}$, e.g. $\boldsymbol{\psi} = [C_{H_2}, C_{H_2O}]$, to parametrize a target quantity Q, e.g. $Q = \dot{\omega}_C$, is quantified by an error norm referred to as irreducible error. This error measures the amount of scatter of Q with respect to the conditional mean if conditioning Q on $\boldsymbol{\psi}$. Consequently, small values of the irreducible error imply a good parametrization of the target quantity by the set of parameters. The irreducible error is defined as

$$\epsilon_{\text{irr}}^2 = \langle\, (Q - \langle Q|\boldsymbol{\psi}\rangle)^2 \,\rangle, \tag{5}$$

where $\langle\rangle$ is an ensemble average and $\langle Q|\boldsymbol{\psi}\rangle$ is the conditional average of Q with respect to $\boldsymbol{\psi}$. In addition to the average irreducible errors, the conditional statistics of the irreducible error with respect to progress variable are studied yielding

$$\epsilon_{\text{irr,C}}^2 = \langle\, (Q - \langle Q|\boldsymbol{\psi}\rangle)^2 \,|\, C_i \,\rangle. \tag{6}$$

The magnitude of $\dot{\omega}_C$ varies among the different cases, so, for comparability, the irreducible errors of the source term are normalized by the maximum value of $\dot{\omega}_C^{\text{Flamelet}}$ in an unstretched flamelet yielding

$$\epsilon_{\text{irr}}^{\text{norm}} = \frac{\epsilon_{\text{irr}}^2}{\max(\dot{\omega}_C^{\text{Flamelet}})^2}, \tag{7}$$

which analogously applies to the conditional irreducible errors $\epsilon_{\text{irr,C}}^{\text{norm}}$.

For the optimal estimator analysis of $\dot{\omega}_C$, the following six different parameters and their combinations are considered: the two progress variables C_{H_2} and C_{H_2O}, the curvature of the flame front κ, the tangential strain rate $\mathcal{K}_S$, the flame stretch $\mathbb{K}$, and mixture fraction Z. The parameters κ, $\mathcal{K}_S$, and $\mathbb{K}$ are defined as

$$\kappa = \nabla \cdot \boldsymbol{n} \tag{8}$$

$$\mathcal{K}_S = \nabla \cdot \boldsymbol{u} - \boldsymbol{n} \cdot \nabla \boldsymbol{u} \cdot \boldsymbol{n} \tag{9}$$

$$\mathbb{K} = \kappa s_d + \mathcal{K}_S, \tag{10}$$

where κ is determined from the divergence of the flame normal vector $\boldsymbol{n} = -\nabla C_i/|\nabla C_i|$ that points towards the unburned and can be determined from any of the two progress variables C_{H_2} and C_{H_2O}. $\boldsymbol{u}$ is the gas velocity, $\nabla \boldsymbol{u}$ is the velocity gradient, and s_d refers to the flame displacement speed of an iso-surface of the progress variable [28]. In particular s_d is defined by

$$s_d = \frac{1}{|\nabla C_i|}\left(\frac{\partial C_i}{\partial t} + u_j \frac{\partial C_i}{\partial x_j}\right), \tag{11}$$

and u_j are the different components of the gas velocity $\boldsymbol{u}$. As shown in the supplementary material, the choice of progress variable to determine κ, $\mathcal{K}_S$, $\mathbb{K}$, and s_d does not affect the irreducible errors of $\dot{\omega}_C$. Hence, κ, $\mathcal{K}_S$, $\mathbb{K}$, and s_d are determined from C_{H_2O} in the following discussion. As thermodiffusive instabilities are linked to strong differential diffusion of hydrogen, the mixture fraction Z has been included into the analysis to highlight the variation of local equivalence ratio within the flame. Z is defined by the Bilger mixture fraction [29] as

$$Z = \frac{Z_H + \nu(Y_{O_2,\text{air}} - Z_O)}{1 + \nu Y_{O_2,\text{air}}}. \tag{12}$$

The stoichiometric coefficient ν is defined by the ratio of the molar masses of oxygen and hydrogen as $\nu = 2M_{H_2}/M_{O_2}$, Z_H and Z_O represent the element mass fractions of hydrogen and oxygen, and $Y_{O_2,\text{air}}$ is the mass fraction of oxygen in air.

Fig. 5 shows the irreducible errors averaged in time and space if parametrizing $\dot{\omega}_C$ by different combinations of the six parameters for case 'Ref' and case 'Tu700'. The blue bars in Fig. 5 represent the irreducible errors if only one parameter (referred to as 1D) is picked to parametrize $\dot{\omega}_C$, while the red (yellow) bars represent parameter sets consisting of two parameters (referred to as 2D) that contain C_{H_2O} (C_{H_2}) and one of the remaining parameters.

For case 'Ref', large non-zero irreducible errors are visible if parametrizing $\dot{\omega}_C$ by one parameter (blue bars), which means that the scatter with respect to the conditional mean $\langle\dot{\omega}_C|\boldsymbol{\psi}\rangle$ for any single parameter $\boldsymbol{\psi}$ is very large. This is consistent with the large scatter of $\dot{\omega}_C$ if conditioned on C_{H_2} that is

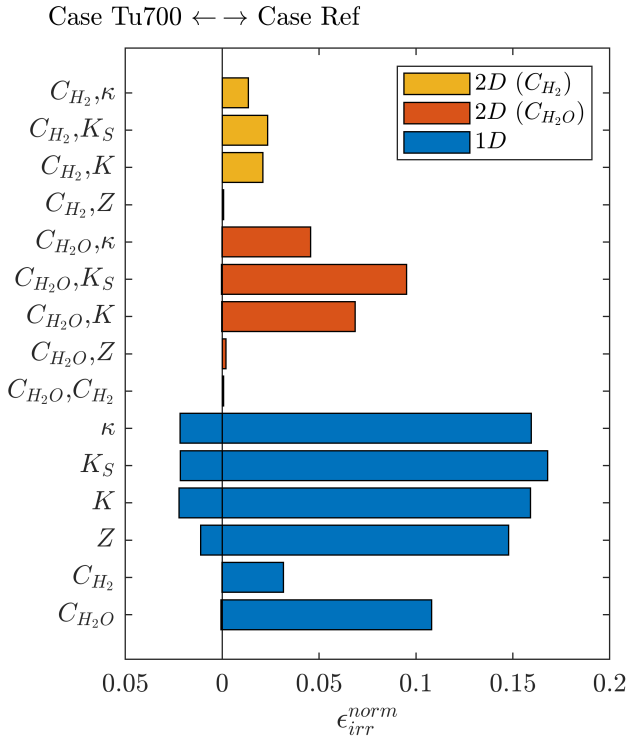

Figure 5: Average irreducible errors of $\dot{\omega}_C$ for different parameter sets $\boldsymbol{\psi}$ for cases 'Tu700' (left) and 'Ref' (right). "1D and 2D" are referring to parameter sets that contain one or two parameters, respectively. Note that for case 'Tu700', several average irreducible errors are close to zero and, hence, are not visible.

shown in Fig. 4. However, vanishing irreducible errors are observed for the parameter combinations $[C_{H_2O}, Z]$, $[C_{H_2}, Z]$, and $[C_{H_2O}, C_{H_2}]$ such that a good parametrization (or small scatter) of $\dot{\omega}_C$ can be achieved if using two parameters. Furthermore, curvature, strain rate, and stretch are found to not parametrize $\dot{\omega}_C$ as well as mixture fraction if used in combination with a progress variable. To further assess this, Fig. 6 shows the irreducible errors conditionally averaged with respect to C_{H_2O} and C_{H_2}. It is worth noting that the integral of the conditionally averaged irreducible errors in Fig. 6 weighted with the PDF $\mathcal{P}(C_{H_2O})$ and $\mathcal{P}(C_{H_2})$, respectively, corresponds to the average

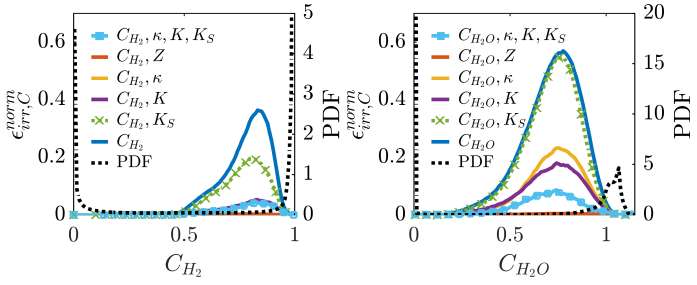

Figure 6: Case 'Ref': Irreducible errors of $\dot{\omega}_C$ for different parameter sets $\boldsymbol{\psi}$ conditionally averaged with respect to C_{H_2} (left panel) and C_{H_2O} (right panel). The black dotted lines represent the PDF $\mathcal{P}(C_{H_2})$ and $\mathcal{P}(C_{H_2O})$, respectively. Note that for the left panel, the yellow, purple, and light blue curve cannot be well distinguished as they are very close to each other.

values displayed in Fig. 5. Consistent with the average irreducible errors, using any of the progress variables leads to large irreducible errors, even though the irreducible errors of C_{H_2} are significantly lower than for C_{H_2O}. Note that maximum irreducible errors and, hence, fluctuations around the mean of about 30% and 60% are observed for C_{H_2} and C_{H_2O}, respectively. Furthermore, it is worth noting that the large discrepancy of the average irreducible errors $\epsilon_{\text{irr}}^{\text{norm}}(C_{H_2}) = 0.032$ and $\epsilon_{\text{irr}}^{\text{norm}}(C_{H_2O}) = 0.11$ in Fig. 5 if using $\boldsymbol{\psi} = [C_{H_2}]$ or $\boldsymbol{\psi} = [C_{H_2O}]$, respectively, is mainly related to the sub- and super-unity values of C_{H_2O} in the burned gas, which do not exist for C_{H_2}. In particular, the value $C_{H_2O} = 1$ corresponds to two characteristic flame states that cannot be distinguished. This value can either correspond to states within the flame, where reaction rates are non-zero and C_{H_2O} keeps increasing, or to points far in the burned gas, where the reaction rates are zero. Hence, the conditional irreducible errors $\epsilon_{\text{irr,C}}^{\text{norm}}(C_{H_2O})$ corresponding to $\boldsymbol{\psi} = [C_{H_2O}]$ are non-zero at $C_{H_2O} = 1$ in Fig. 6 indicating a scatter of $\dot{\omega}_C$ at this value as the aforementioned two flame states are not distinguished. Since the probability of finding $C_{H_2O} = 1$ within the computational domain is high as it includes a large fraction of the burned gases, relatively high average irreducible errors are obtained for C_{H_2O} in Fig. 5. Additionally, the conditional irreducible errors clearly reveal that curvarture, strain rate, and stretch do not reduce irreducible errors as much as mixture fraction if used in combination with a progress variable. In particular, Fig. 6 also shows the irreducible errors of the parameter sets $\boldsymbol{\psi} = [C_i, \kappa, \mathcal{K}_S, \mathbb{K}]$, where all four parameters are used, but still larger irreducible errors are obtained compared to the set $\boldsymbol{\psi} = [C_i, Z]$. This will be discussed in detail at the end of this section.

For case 'Tu700', Fig. 5 yields vanishing irreducible errors if parametrizing $\dot{\omega}_C$ by any of the progress variables, which is consistent with the vanishing scatter of $\dot{\omega}_C$ with respect to C_{H_2} in Fig. 4. Thus, the combustion process of case 'Tu700' is already well parametrized by only one parameter.

As any of the combinations $[C_{H_2O}, Z]$, $[C_{H_2}, Z]$, and $[C_{H_2O}, C_{H_2}]$ adequately parametrizes $\dot{\omega}_C$ and allows for an unambiguous description of the local flame state, the following discussion will be based on $[C_{H_2O}, Z]$ as the effects of differential diffusion can be well explained by mixture fraction and in contrast to C_{H_2}, the choice of C_{H_2O} provides insights into the variation of the C_{H_2O} overshoots in the burned gases at different conditions. Joint PDFs of the other two combinations, by which the flame state can be equally well studied, are provided in the supplementary material.

The left column of Fig. 7 shows the joint PDF of C_{H_2O} and $\dot{\omega}_C$ for selected cases. Additionally, the conditional average $\langle \dot{\omega}_C | C_{H_2O} \rangle$ and the unstretched premixed flamelet are shown. A strong scatter of $\dot{\omega}_C$ with respect to C_{H_2O} and strong discrepancies with respect to the unstretched flamelet are seen for the strongly unstable cases 'Ref' and 'p10'. In particular, two branches of reaction rates can be identified: one branch of enhanced reactivity and one branch of strongly reduced or vanishing reactivity compared to the unstretched flamelet. These two reaction branches result from the differential diffusion of hydrogen along the flame front, which leads to the formation

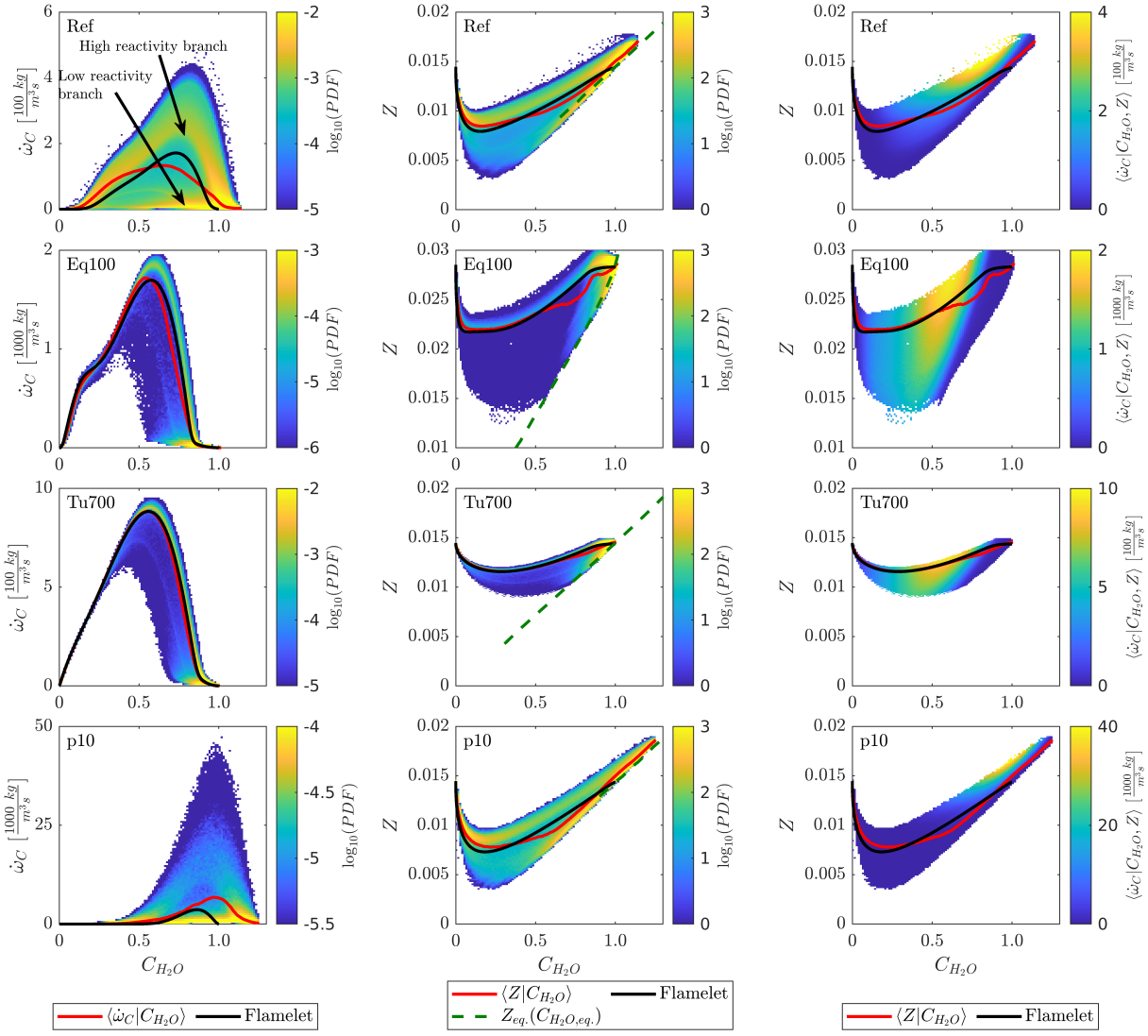

Figure 7: Left column: Joint PDF of $\dot{\omega}_C$ and C_{H_2O}, $\dot{\omega}_C$ conditionally averaged on C_{H_2O} (red line), and flamelet solution (black line). Middle column: Joint PDF of Z and C_{H_2O}, Z conditionally averaged on C_{H_2O} (red line), flamelet solution (black line), and dependence of $C_{H_2O,eq}$ on Z at equilibrium conditions (green line). Right column: Conditional mean of $\dot{\omega}_C$ with respect to Z and C_{H_2O}, Z conditionally averaged on C_{H_2O} (red line), and flamelet solution (black line).

of locally richer and leaner mixtures. This becomes evident from the joint PDFs $\mathcal{P}(C_{H_2O}, Z)$ shown in the middle column of Fig. 7, where one branch is above and the other branch is below the unstretched flamelet. Due to the variation of the local equivalence ratio, the combustion process of the two branches terminates at different progress variable values. This is indicated by the green dotted line, which represents the progress variable $C_{H_2O,eq}$ at thermodynamic equilibrium for a given mixture fraction Z_{eq}. $C_{H_2O,eq}$ is defined as

$$C_{H_2O,eq} = Y_{H_2O,eq}(Z_{eq}) / Y_{H_2O,b}, \tag{13}$$

where the mass fraction of water at equilibrium $Y_{H_2O,eq}$ depends on the mixture fraction Z_{eq} and it is normalized by the mass fraction of water $Y_{H_2O,b}$ in the burned gas for each case (this value differs among the cases but is constant for each of the green lines in the middle column of Fig. 7). Further, the green lines terminate at low values of Z_{eq}, when the flammability limit of an unstretched laminar flamelet is reached. For all cases, the green lines agree well with a line of high probability values of the joint PDF $\mathcal{P}(C_{H_2O}, Z)$. These states represent the long trails of sub- and super-unity values of C_{H_2O} in the post-flame region, as the lower/upper branch locally burn at leaner/richer conditions. Note that the unstretched flamelet terminates at $C_{H_2O} = 1$. The right column of Fig. 7 shows the conditional average of the progress variable source term $\dot{\omega}_C$ with respect to C_{H_2O} and Z. For the cases 'Ref' and 'p10', $\dot{\omega}_C$ significantly varies with respect to C_{H_2O} and Z such that small fluctuations in C_{H_2O} and Z due to differential diffusion lead to a significant variation of $\dot{\omega}_C$ as visible in the first column of Fig. 7.

For cases 'Eq100' and 'Tu700', a significant reduction of the scatter and a value of $\dot{\omega}_C$ much closer to the flamelet solution are observed even though the existence of the two characteristic

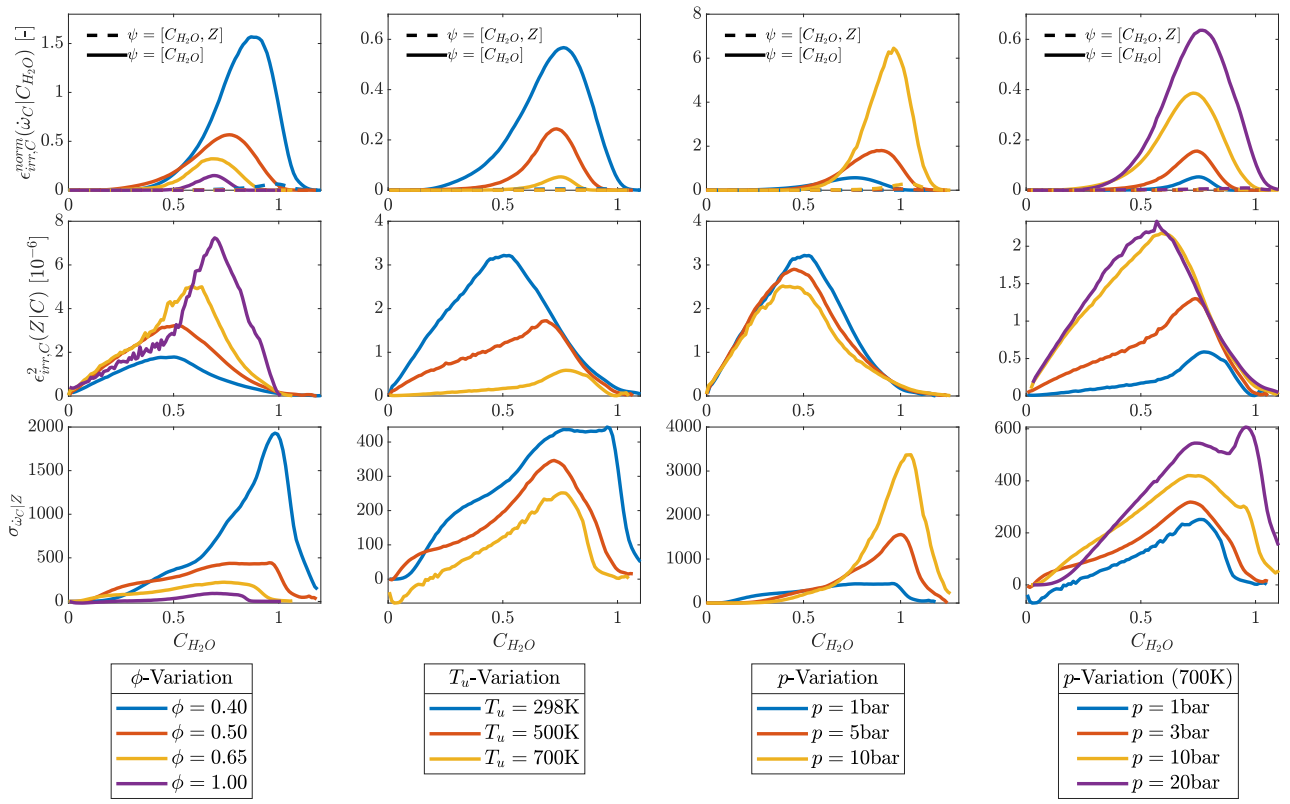

Figure 8: Top row: Irreducible errors of the progress variable source term $\dot{\omega}_C$ parametrized by progress variable C_{H_2O} (solid lines) and by progress variable and mixture fraction $[C_{H_2O}, Z]$ (dashed lines). Middle row: Irreducible errors of mixture fraction Z parametrized by progress variable C_{H_2O} (solid lines). Bottom row: Sensitivity of progress variable source term $\dot{\omega}_C$ with respect to mixture fraction Z conditionally averaged against progress variable C_{H_2O}.

branches is still weakly visible. Particularly for case 'Eq100', significant fluctuations of mixture fraction are still visible in the joint PDF $\mathcal{P}(C_{H_2O}, Z)$ but the reduced scatter of $\dot{\omega}_C$ results from a reduced sensitivity of $\dot{\omega}_C$ with respect to Z as can be seen from the right column of Fig. 7, which will be quantified in the following. For case 'Tu700', a reduction of mixture fraction fluctuations and a reduced sensitivity of $\dot{\omega}_C$ with respect to Z are observed yielding a relatively uniform distribution of $\dot{\omega}_C$ along the flame front. Further, if comparing the joint PDFs $\mathcal{P}(C_{H_2O}, Z)$ of all cases in Fig. 7, it becomes evident that the progress variable overshoots are significantly enhanced towards unstable conditions, which will be further discussed at the end of this section.

The above findings can be quantitatively confirmed by means of an irreducible error analysis for the different parameter variations similar to the depiction for the reference case in Fig. 6. For this, in the top row of Fig. 8, the normalized irreducible error of $\dot{\omega}_C$ with respect to $\boldsymbol{\psi} = [C_{H_2O}]$ (solid lines) and $\boldsymbol{\psi} = [C_{H_2O}, Z]$ (dashed lines) is shown conditionally averaged with respect to C_{H_2O}. The reduction of irreducible errors towards stable conditions if using the parameter set $\boldsymbol{\psi} = [C_{H_2O}]$ indicates a reduction of source term fluctuations for all cases while the near-zero irreducible errors for the parameter set $\boldsymbol{\psi} = [C_{H_2O}, Z]$ indicate the good parametrization of $\dot{\omega}_C$ by these two parameters even for the strongly unstable cases. As the source term fluctuations arise from mixture fraction fluctuations, in the middle row of Fig. 8, the (unnormalized) conditionally averaged irreducible errors of Z parametrized by C_{H_2O} are shown. Consistent with the previous qualitative analysis, an increase of equivalence ratio or pressure at elevated temperature increases mixture fraction fluctuations and hence irreducible errors, while the increase of unburned temperatures reduces mixture fraction fluctuations. Note that for the pressure increase at ambient temperatures, only a minor reduction of mixture fraction fluctuations is visible. Finally, to link the mixture fraction fluctuations to the source term fluctuations, the sensitivity of $\dot{\omega}_C$ with respect to Z fluctuations at a given value of C_{H_2O} is needed. For this, the sensitivity $\sigma_{\dot{\omega}_C|Z}$ describing the variability of the progress variable source term with respect to mixture fraction is shown in the bottom row of Fig. 8. The sensitivity $\sigma_{\dot{\omega}_C|Z}$ is defined as

$$\sigma_{\dot{\omega}_C|Z} = \frac{1}{\max(\dot{\omega}_C^{\text{Flamelet}})} \cdot \frac{\partial \left[\langle \dot{\omega}_C | C_{H_2O}, Z \rangle\right]}{\partial Z}\bigg|_{C_{H_2O}}, \tag{14}$$

where the partial derivative represents the variation of the conditionally averaged source term $\langle \dot{\omega}_C | C_{H_2O}, Z \rangle$ with respect to Z at a constant value of C_{H_2O}. If this variability is small, mixture fraction fluctuations do not significantly affect the source term value. It is worth noting that the variability is normalized by the peak source term value of an unstretched flamelet to compare $\sigma_{\dot{\omega}_C|Z}$ among the different cases. Thus, since the increase of equivalence ratio leads to a significant reduction of $\sigma_{\dot{\omega}_C|Z}$, a reduction of $\dot{\omega}_C$ fluctuations is observed even though mixture fraction flucutations increase towards higher equivalence ratios. For increasing pressures at ambient temperatures, Fig. 8 shows

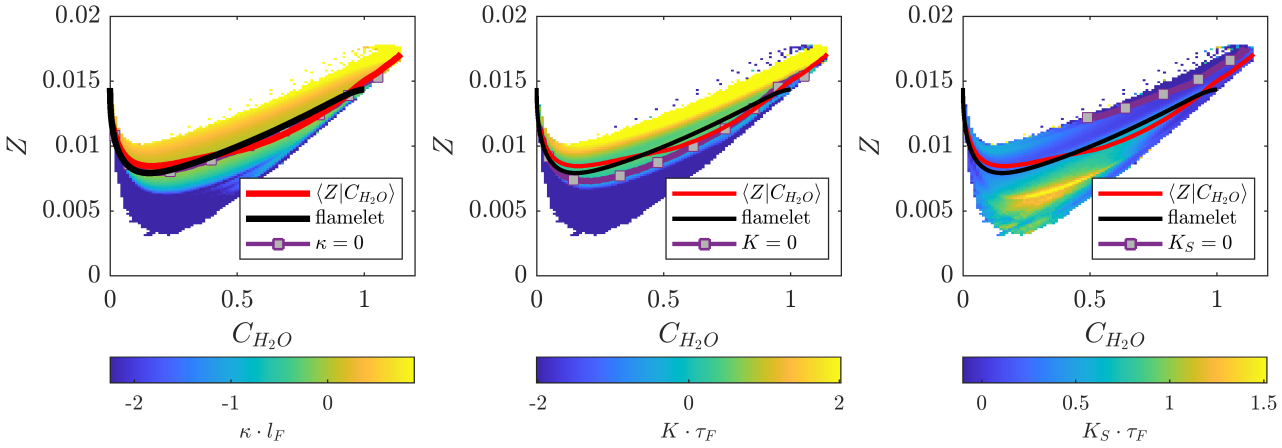

Figure 9: Case 'Ref' (from left to right): Curvature, stretch, and strain rates conditionally averaged with respect to C and Z. Additionally, the conditional average (red line) and flamelet solution (black line) of mixture fraction Z and progress variable C, and the line of zero curvature, stretch, and strain rates values is shown.

that the increase of source term fluctuations at ambient temperature mainly arises from an increase of sensitivity $\sigma_{\dot{\omega}_C|Z}$ as mixture fraction fluctuations do not significantly differ at different pressures. Instead, for the decrease of unburned temperature and the increase of pressure at elevated temperatures, both mixture fraction fluctuations and the sensitivity $\sigma_{\dot{\omega}_C|Z}$ increase yielding a stronger scatter of $\dot{\omega}_C$.

In the following, the discrepancy of mixture fraction and the topological parameters such as curvature κ, strain rate $\mathcal{K}_S$, and stretch $\mathbb{K}$ in parametrizing $\dot{\omega}_C$ according to the optimal estimator analysis and the relationship among these parameters is discussed. Fig. 9 shows κ, $\mathcal{K}_S$, and $\mathbb{K}$ conditionally averaged with respect to C_{H_2O} and Z. Note that κ, $\mathcal{K}_S$, $\mathbb{K}$ are determined from C_{H_2O} but no significant differences are observed if using C_{H_2} for their determination as shown in the supplementary material. The upper reaction branch of higher mixture fraction values observed in Fig. 7 corresponds to flame segments that are convexly curved towards the unburned (positive curvature values) and the lower branch corresponds to concavely curved flame front segments, which correspond to the cusp regions along the flame front. Furthermore, Fig. 9 displays the line of zero curvature values, which is close to the unstretched flamelet solution and indicates that the departure from the unstretched flamelet to lower and higher mixture fraction values correlates well with a decrease or increase of curvature. A similar trend is seen for the stretch rates but not for the strain rate, which has no significant impact as can be also seen from the insignificant reduction of irreducible errors in Fig. 6 if comparing the parameter sets $\boldsymbol{\psi} = [C_{H_2O}]$ and $\boldsymbol{\psi} = [C_{H_2O}, \mathcal{K}_S]$. Hence, while the differential diffusion of hydrogen lateral to the flame front originates from the topological deformation of the flame, the irreducible error analysis demonstrates that the local flame state is not fully described by the instantaneous topological parameters such as curvature, strain rate, or stretch. As suggested by Klimenko et al. [30], the parametrization of the local flame state may require additional parameters such as the rate of change of curvature, or more generally, the history of the flame front evolution. Thus,

Table 2: Assessment of temperature overshoots in the burned gas for the different cases. The table provides the adiabatic flame temperature T_b, the maximum observed temperature max(T), and the difference with respect to the peak temperature $\Delta T_{\text{Overshoot}} = (\max(T) - T_b)$.

Case name	T_b [K]	max(T) [K]	$\Delta T_{\text{Overshoot}}$ [K]
Ref	1643	1814	171
Eq040	1418	1630	212
Eq065	1930	2002	72
Eq100	2316	2389	73
Tu500	1809	1858	49
Tu700	1971	2006	35
p05	1644	1916	272
p10	1643	1917	274
Tu700p03	1977	2023	46
Tu700p10	1980	2161	181
Tu700p20	1980	2201	221

while curvature and mixture fraction are strongly linked to each other as demonstrated in Fig. 7, mixture fraction is found to parametrize the local flame state significantly better compared to the topological parameters as mixture fraction fluctuations represent the result of differential diffusion while the topological parameters, such as curvature, only represent the cause of differential diffusion and their effect on the flame state may not be prompt but delayed.

Finally, the super-adiabatic values of C_{H_2O}, which correspond to temperature overshoots beyond the adiabatic temperature, are known to occur for sub-unity Lewis number flames that are positively stretched as shown by Giannakopoulos et al. [31]. Hence, the enhancement of peak temperatures can be used as a marker for the strength of the thermodiffusive instability mechanism and indeed, in Figs. 8 and 7, the peak values of C_{H_2O} reduce towards stable conditions. This is quantitatively shown in Tab. 2, where the adiabatic flame temperature T_b, the max-

imum observed temperature max(T), and the difference with respect to the peak temperature $\Delta T_{\mathrm{Overshoot}} = (\max(T) - T_{\mathrm{b}})$ are compared. For this comparison, temperature is chosen instead of $C_{\mathrm{H_2O}}$ as temperature overshoots are relevant for the thermal formation of $\mathrm{NO_x}$ emissions. For instance, it is worth noting that for case 'Tu700p20' at high pressures and elevated temperatures, which is close to gas turbine conditions, temperature overshoots up to 221 K are visible, which can significantly impact $\mathrm{NO_x}$ emissions.

3.3. Flame Speed Analysis: Consumption Speed

Flame front wrinkling and the variations of reaction rates can lead to a significantly higher flame speed compared to planar, unstreched laminar flames, which is discussed in the following. An integral measure of flame speed is given by the consumption speed s_{c} defined as

$$s_{\mathrm{c}} = -\frac{1}{\rho_{\mathrm{u}} Y_{\mathrm{H_2,u}} L_{\mathrm{x}}} \int \dot{\omega}_{\mathrm{H_2}} \mathrm{d}x\mathrm{d}y, \tag{15}$$

where ρ_{u} and $Y_{\mathrm{H_2,u}}$ are the density and fuel mass faction in the unburned mixture, L_{x} is the width of the two-dimensional computational domain, $\dot{\omega}_{\mathrm{H_2}}$ is the consumption rate of fuel due to chemical reactions, and $\int \mathrm{d}x\mathrm{d}y$ represents the integral over the entire two-dimensional computational domain. Berger et al. [11] have shown that for a sufficiently large domain width L_{x}, a constant value of the consumption speed is obtained. Berger et al. [11] identified a minimum domain size of $L_{\mathrm{x}} = 100 l_{\mathrm{F}}$ for case 'Eq040'. Similar findings are also reported by Creta et al. [22] for thermodiffusively unstable flames. Therefore, all performed simulations possess domain widths $L_{\mathrm{x}} \geq 100 l_{\mathrm{F}}$ to reliably determine the consumption speed.

Fig. 10 shows the average consumption speed of the different cases normalized by the laminar unstretched flame speed s_{L} after the statistically steady state is reached. For unstable conditions, a significant increase of the ratio $s_{\mathrm{c}}/s_{\mathrm{L}}$ is observed as the thermodiffusive instability mechanism affects the flame front wrinkling and flame burning behavior. To understand the causes of the flame speed increase, the consumption speed is expressed as

$$s_{\mathrm{c}} = s_{\mathrm{L}} \frac{\Sigma}{L_{\mathrm{x}}} I_0 \tag{16}$$

showing that a deviation from the laminar unstretched flame speed s_{L} arises either from an increase of flame surface area Σ due to wrinkling or from a deviation of the local burning rate with respect to an unstretched flamelet. The latter aspect is accounted for by the factor I_0 and describes the overall change in reactivity. Σ is defined as the surface area of an iso-surface of progress variable with value $C_{\mathrm{i}} = C_0$ and according to Vervisch et al. [32] is given as

$$\Sigma = \int |\nabla C_{\mathrm{i}}| \, \delta(C_{\mathrm{i}} - C_0) \mathrm{d}x\mathrm{d}y, \tag{17}$$

by employing the Dirac δ-function. It is worth noting that Σ possesses units of a length due to the two-dimensional configuration. For thin flames, the value of Σ does not depend on the

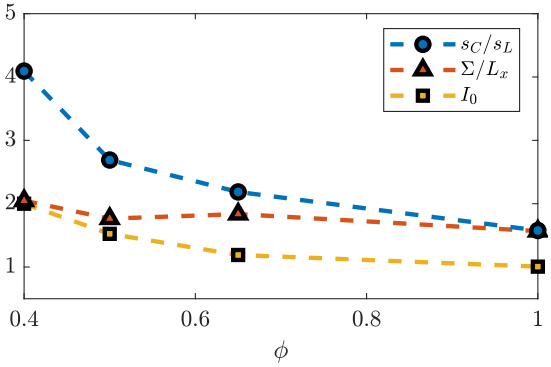

(a) ϕ-Variation

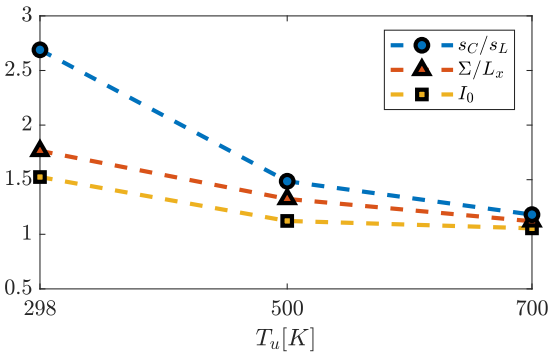

(b) T_u-Variation

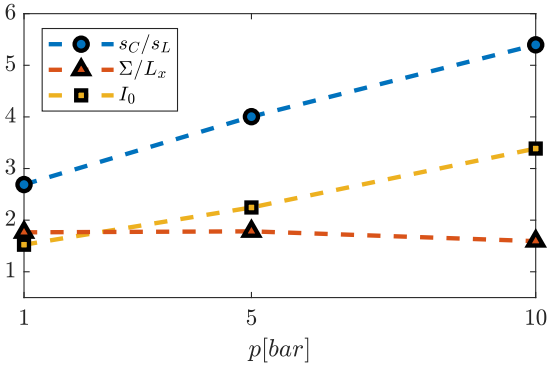

(c) p-Variation

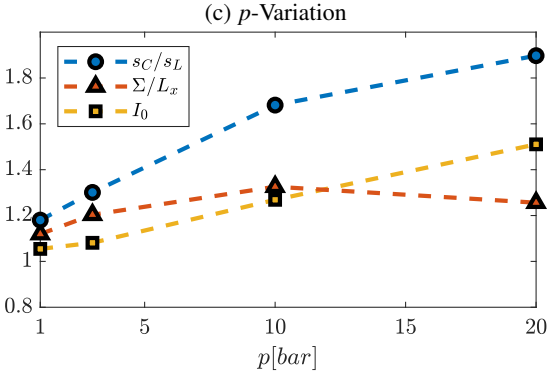

(d) p-Variation at 700K

Figure 10: Variation of the consumption speed s_{C} normalized by the laminar unstretched burning velocity s_{L}, the flame surface area Σ normalized by the lateral domain width L_{x}, and the factor I_0 with respect to the different parametric variations of equivalence ratio ϕ, unburned temperature T_{u}, pressure p, and pressure at elevated unburned temperatures $p(700K)$.

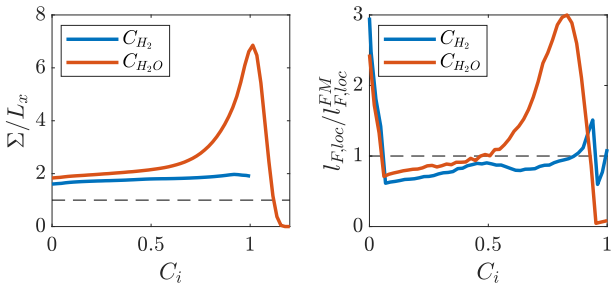

(a) Case 'Ref'

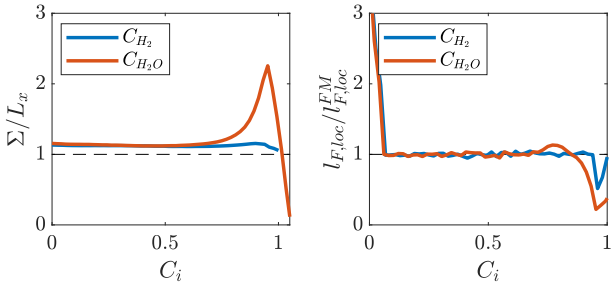

(b) Case 'Tu700'

Figure 11: Determination of flame surface area and the local flame thickness by progress variable iso-lines and iso-lines of the hydrogen mass fraction field.

choice of iso-surface C_0. However, it is worth noting that the choice of progress variable and C_0 can significantly affect the values in Fig. 10, which is discussed in the following.

For cases 'Ref' and 'Tu700', Fig. 11 shows the value of Σ determined for different choices of C_0 and for both progress variables C_{H_2O} and C_{H_2}. For both flames, a significant increase of Σ for high values of C_0 is observed if evaluating Eq. 17 from C_{H_2O} even though the variability of Σ with respect to C_0 is lower for case 'Tu700'. In contrast, a flat curve is seen if evaluating Σ from C_{H_2} such that the choice of iso-surface C_0 does not affect its value. Thus, Σ will be determined by C_{H_2} in the following. The increase of Σ for high values of C_0, if determined from C_{H_2O}, results from the long trails of sub- and super-unity values of C_{H_2O} in the post flame region, which are visible in Fig. 3. This leads to a significant thickening of the C_{H_2O} iso-surfaces as will be shown in the subsequent paragraph and, hence, to an increase of flame surface area towards the burned. As the hydrogen fields do not possess these long trails of sub- and super-unity values in the burned gas, a constant value of Σ is obtained.

Prior to the discussion of the consumption speed, surface area increase, and the factor I_0 in the next paragraph, it is worth noting that the global consumption speed and I_0 are not only affected by the variations of the local reaction rates, but also by the variations of the local flame thickness as the flame volume, in which the fuel is consumed, depends on the flame surface area and flame thickness. This is briefly discussed in the following. The local flame thickness is determined by computing the volume (or 'area' in 2D) between two iso-surfaces of progress variable, which is normalized by the flame surface area (or 'length' in 2D), and is defined as [33]

$$l_{\mathrm{F,loc}} = \frac{1}{\Delta C \cdot \Sigma} \int H(C_{\mathrm{i}} - C_{-}) H(C_{+} - C_{\mathrm{i}})\, \mathrm{d}x\mathrm{d}y. \qquad (18)$$

ΔC is the separation of progress variable values among the two iso-surfaces that are defined by $C_+ = (C_0 + \Delta C/2)$ and $C_- = (C_0 - \Delta C/2)$, respectively, and $H()$ represent the Heaviside function. ΔC is set to $\Delta C = 0.1$, but no significant variations are seen for other values of ΔC as long as they are small enough. In Fig. 11, the local flame thickness is normalized by $l_{\mathrm{F,loc}}^{\mathrm{FM}}$, which is the local thickness of an unstretched laminar flame determined by Eq. 18. Note that the local flame thicknesses $l_{\mathrm{F,loc}}$ and $l_{\mathrm{F,loc}}^{\mathrm{FM}}$ become zero in the burned and unburned, so the ratio $l_{\mathrm{F,loc}}/l_{\mathrm{F,loc}}^{\mathrm{FM}}$ is not well defined and is prone to numerical errors for $C_{\mathrm{i}} \to 0$ and $C_{\mathrm{i}} \to 1$. Consistent with the flame surface area increase at high values of C_0 for case 'Ref', a significant increase of flame thickness is seen towards the burned gas in Fig. 11 if using $C_{\mathrm{H_2O}}$ to evaluate Eq. 18 as the distance between two iso-surfaces increases in the burned gas due to the long trails of sub- and super unity values of $C_{\mathrm{H_2O}}$. In contrast, no increase of flame thickness is seen at high values of C_0 in Fig. 11 if using $C_{\mathrm{H_2}}$ to evaluate Eq. 18 for case 'Ref'. Fig. 12 shows the local flame thickness normalized by the value obtained in the corresponding unstretched flamelet and determined from $C_{\mathrm{H_2}}$ for all cases. Towards unstable conditions, an overall reduction of the local flame thickness compared to the flamelet solution is seen, which is particularly strong for small values of $C_{\mathrm{H_2}}$, while towards stable conditions, the local flame thickness is close to the flamelet solution. Hence, in the strongly unstable cases, reaction rates occur in thinner flame fronts compared to an unstretched flame, which will be picked up in the following discussion related to the factor I_0. Finally, note that for the stoichiometric case 'Eq100' with $\phi = 1$, differential diffusion leads to locally rich mixtures such that the fuel is not fully con-

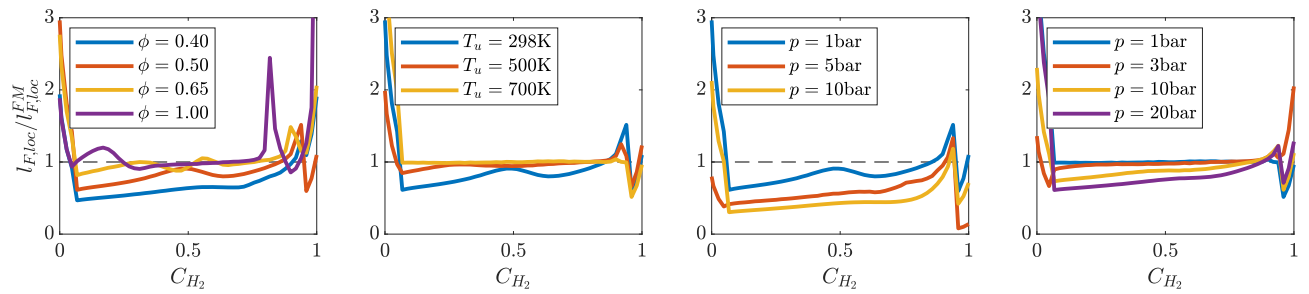

Figure 12: Variation of the local flame thickness determined from iso-lines of the hydrogen mass fraction field for the different parametric variations of equivalence ratio ϕ, unburned temperature T_{u}, pressure p, and pressure at elevated unburned temperatures $p(700K)$.

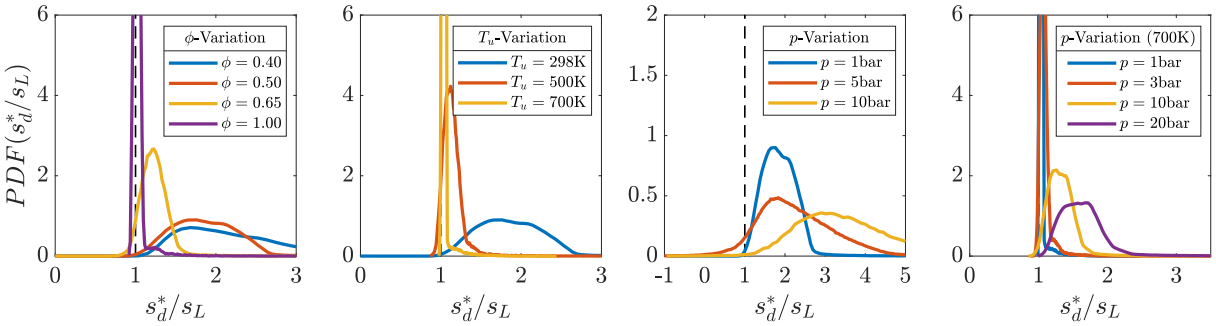

Figure 13: Variation of the PDF of the flame displacement speed s_d^* normalized by the unstretched laminar burning velocity s_L and evaluated from $C_{\mathrm{H_2O}} = 0.6$ for the different parametric variations of equivalence ratio ϕ, unburned temperature T_u, pressure p, and pressure at elevated unburned temperatures $p(700K)$.

sumed behind the flame front. This leads to regions behind the flame front, in which hydrogen is non-zero, which in turn leads to the spike of flame thickness towards the burned gas for case 'Eq100' in Fig. 12.

To assess the relevance of flame wrinkling and effects due to variations of reactivity on the flame consumption speed, Fig. 10 shows the values of Σ/L_x and I_0 in addition to $s_\mathrm{c}/s_\mathrm{L}$. For the variations of equivalence ratio and unburned temperature, an increase of both Σ/L_x and I_0 is observed towards unstable conditions and unity values of I_0 are obtained towards stable conditions. Thus, for cases 'Eq100' and 'Tu700', the unity values of I_0 indicate a local burning behavior that is close to an unstretched flamelet. Note that I_0 contains the effects of reaction rate and flame thickness variations and since reaction rates are shown to be in good agreement with the values of an unstretched flamelet, cf. Fig. 7, it can be concluded that the local flame structure is close to an unstretched flamelet. For the variation of pressure at low unburned temperature, the flame front wrinkling remains roughly constant during the increase of pressure while I_0 shows a linear increase. Similarly, for the variation of pressure at elevated unburned temperatures, the flame front wrinkling increases initially but levels off towards higher pressure values while I_0 keeps increasing. Hence, the increase of pressure is found to mainly affect the flame's reactivity rather than its wrinkling. The increase of reactivity relates to the increased sensitivity $\sigma_{\dot{\omega}_\mathrm{C}|Z}$ of the reaction rate $\dot{\omega}_\mathrm{C}$ to mixture fraction and an increase of mixture fraction fluctuations for higher pressures as quantified in Fig. 8. Hence, larger deviations of the mixture fraction from the value of an unstretched laminar flamelet are observed at higher pressures, which have an even stronger effect on the reaction rates, yielding an overall increase of the reactivity and the factor I_0. Finally, it is worth noting that for the strongly unstable cases, e.g. case 'Ref', a super-unity value of I_0 means that the reduction of flame thickness towards the unburned in Fig. 12 is more than compensated by an even stronger increase of reaction rates, when compared to an unstretched flamelet. In other words, the fuel consumption occurs in a thinner flame front while the integral fuel consumption rate per flame surface area (which is I_0) is larger compared to an unstretched flamelet, so fuel consumption rates are high enough to more than compensate the reduction of flame thickness.

3.4. Flame Speed Analysis: Flame Displacement Speed

After having studied the variation of the consumption speed, this section discusses the impact of intrinsic instabilities on the local flame displacement speed. Fig. 13 shows the PDF of the flame displacement speed determined from $C_{\mathrm{H_2}}$. The flame front is defined as $C_0 = 0.6$, but conclusions do not change for other values of C_0 or if pursuing this analysis for the displacement speed determined from $C_{\mathrm{H_2O}}$ as shown in the supplementary material. For reference, the flame displacement speed is normalized by the laminar unstretched burning velocity of each case and the displacement speed s_d is corrected by the densities of the iso-surface ρ_iso and the unburned ρ_u yielding [31]

$$s_\mathrm{d}^* = \frac{\rho_\mathrm{iso} s_\mathrm{d}}{\rho_\mathrm{u}}, \tag{19}$$

such that s_d^* would be unity for any iso-surface in an unstretched laminar flame. Towards stable conditions, such as cases 'Eq100' or 'Tu700', s_d^* is found to possess a very narrow distribution around the value of the laminar unstretched burning velocity indicating that the local flame propagation is not significantly affected by the flame front wrinkling and is similar to an unstretched flamelet. However, towards unstable conditions, a significant broadening of the PDF is seen and s_d^* significantly deviates from the unstretched laminar burning velocity as variations of composition along the flame front due to differential diffusion become increasingly important. Hence, the broadening of the PDFs of s_d^* shows the impact of the flame front corrugations on the local flame propagation and is consistent with the increasing value of I_0 for highly unstable conditions.

It is worth noting that the variations of the flame displacement speed from the laminar unstretched burning velocity arise from the mixture fraction fluctuations, which is consistent with the source term analysis of $\dot{\omega}_\mathrm{C}$. For case 'Ref', Fig. 14 (a) shows the joint PDF of s_d^* and Z. For reference, the mixture fraction value Z_flamelet of an unstretched flamelet is displayed and most of the mixture fraction values are seen to be larger than Z_flamelet. In particular, these points represent flame segments that are positively curved and belong to the branch of enhanced reactivity as discussed in Fig. 9. This can be also seen from the joint PDF of s_d^* and curvature κ shown in Fig. 14 (b). Furthermore, also the joint PDF of s_d^* and strain rate $\mathcal{K}_\mathrm{S}$ is shown and for each subfigure, two dotted lines representing a confidence interval of 90% of the conditional PDFs $\mathcal{P}(s_\mathrm{d}^*|Z)$,

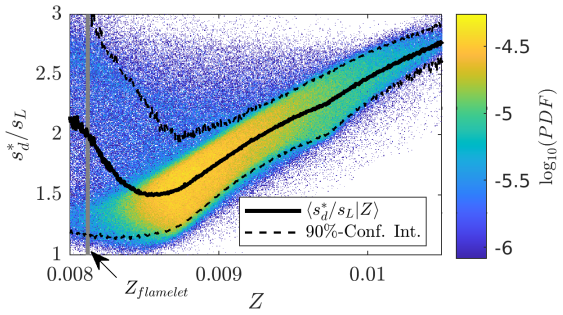

(a) Joint PDF of s_d^* and Z

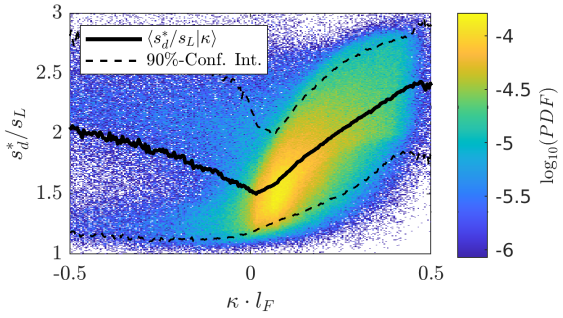

(b) Joint PDF of s_d^* and κ

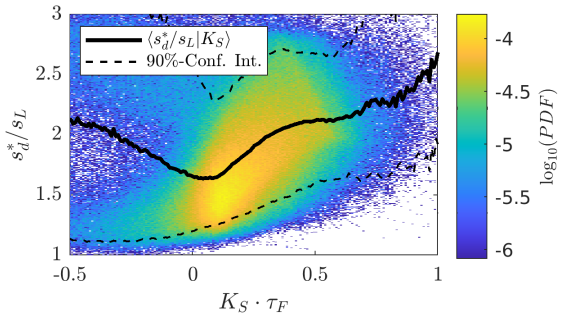

(c) Joint PDF of s_d^* and $\mathcal{K}_S$

Figure 14: Case 'Ref': Joint PDF of the flame displacement speed s_d^* of an iso-surface $C_{H_2} = 0.6$ normalized by the laminar unstretched burning velocity s_L and mixture fraction Z (a), curvature κ (b), or strain rate $\mathcal{K}_S$ (c). The black solid line represents the conditional mean and the two dotted lines represent a confidence interval of 90% of the conditional PDF $\mathcal{P}(s_d^*|\psi)$, where ψ is Z, κ, or $\mathcal{K}_S$. The grey line in (a) represents the value of mixture fraction of an unstretched flamelet at $C_{H_2} = 0.6$.

$\mathcal{P}(s_d^*|\kappa)$, and $\mathcal{P}(s_d^*|\mathcal{K}_S)$ are displayed to assess the scatter of s_d^*. Consistent with the source term analysis, mixture fraction yields the lowest scatter of s_d^* and is best suited to parametrize s_d^* as larger scatters are seen for the joint PDFs involving κ and $\mathcal{K}_S$. Consequently, as the reactivity of the local flame segments increases with increasing mixture fraction, super-unity values of s_d^* are obtained. However, it is worth noting that for low value of mixture fraction $Z \lesssim 0.0085$, the scatter of s_d^* significantly increases while yielding also super-unity values of s_d^*. For these regions of lower equivalence ratio, which belong to the cusp regions of the flame front, where reaction rates vanish, s_d^* is dominated by the diffusion term rather than the reaction term of the transport equation of C_{H_2}, which is not well parametrized by Z anymore yielding the large scatter (note that this does not affect the irreducible error analysis of $\dot{\omega}_C$ since $\dot{\omega}_C \approx 0$ in these regions). Hence, the strong diffusive effects in the cusp region compensate the vanishing reaction rates yielding again super-unity values of s_d^*.

3.5. Flame Surface Area and Cellular Structures

Finally, it is assessed whether the flame surface area increase towards unstable conditions arises from small-scale or large-scale flame front wrinkling. Therefore, the size of the smallest cells is measured by means of the curvature along the flame front similar to Berger et al. [11]. In particular, the cusps along the flame front are characterized by distinct spikes of curvature, which enables a robust measurement of the arc distance l^* of the cellular structure between two cusps. Assuming the cellular structures form a semi-circle, a characteristic cell size $\lambda_{cell} = 2l^*/\pi$ is determined. However, while λ_{cell} quantifies the size of the smallest cells, it is worth noting that large scale structures such as the flame fingers, which are overlaid by several small cells, cannot be detected by such an analysis. Fig. 15 shows the PDF of λ_{cell} for the different cases evaluated from an iso-line of C_{H_2} defined by $C_0 = 0.6$; conclusions do not change for other values of C_0 or if pursuing this analysis for C_{H_2O} as shown in the supplementary material.

A shift of the PDFs towards smaller values of λ_{cell} is observed if unstable conditions are approached such that it may be concluded that the size of the cellular structures decreases for unstable conditions. All PDFs are seen to peak at a characteristic wave length $\lambda_{cell,max}$ with $5l_F \lesssim \lambda_{cell,max} \lesssim 9l_F$ and a strong

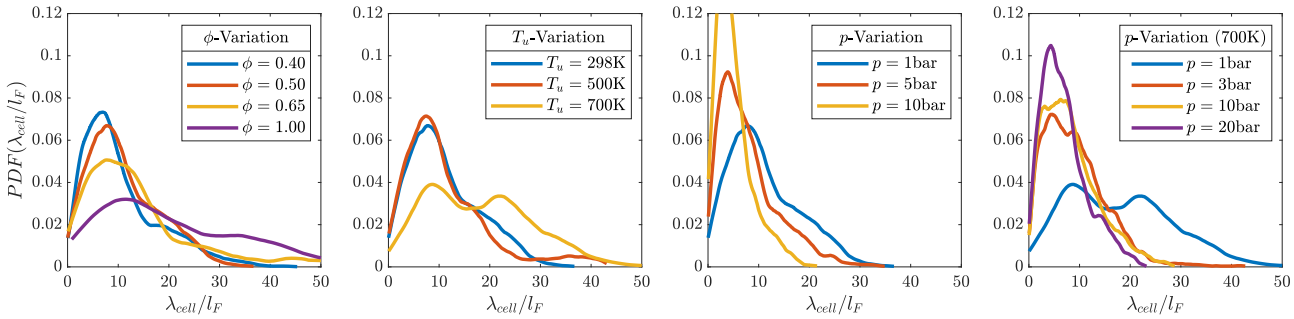

Figure 15: Variation of the PDF of the cell size λ_{cell} of the small cellular structures for the different parametric variations of equivalence ratio ϕ, unburned temperature T_u, pressure p, and pressure at elevated unburned temperatures $p(700K)$.

reduction of probability towards smaller values of λ_{cell} is observed. It is worth noting that the value of $\lambda_{\text{cell,max}}$ is close to the wave length of the maximum growth rate of the dispersion relations $\lambda_{\omega_{\text{max}}}$, which is slightly smaller with $4.5 l_{\text{F}} \lesssim \lambda_{\omega_{\text{max}}} \lesssim 5.6 l_{\text{F}}$. Furthermore, it is worth noting that case 'Tu700' reveals a second peak at $\lambda_{\text{cell}} \approx 22 l_{\text{F}}$, whose origin is yet unclear, but possibly relates to the hydrodynamic instability mechanism, which is affected by the lateral computational domain size as it does not possess a characteristic wave length. However, a variation of domain size would be required to answer this question, which is outside of the scope of this paper.

4. Visualization of Instability Trends

In this section, the flame speed in the non-linear phase is linked to the peak growth rates of the dispersion relations discussed in part 1 of this work [1] and the relevance of intrinsic flame instabilities at different conditions is assessed.

For both the peak growth rate ω_{max} of the dispersion relation in the linear and the ratio of the consumption speed s_{c} relative to the laminar unstretched burning velocity s_{L} in the non-linear regime, an increase is observed towards more unstable conditions. In particular, Fig. 16 shows a good correlation among these two values and a strong link between the characteristic quantities of the linear and non-linear phase that are used to describe the impact of instabilities. Towards stable conditions, the ratio $s_{\text{c}}/s_{\text{L}}$ is seen to tend towards unity and the peak growth rate ω_{max} approaches a value of zero. To assess the scaling behavior of $s_{\text{c}}/s_{\text{L}}$ on ω_{max}, while considering the aforementioned asymptotic limits, the following scaling law is studied

$$\frac{s_{\text{c}}}{s_{\text{L}}} - 1 \propto \omega^{\zeta}, \tag{20}$$

If using all cases for a least-square fit, the coefficient ζ is found to be $\zeta = 1.63 \approx 5/3$ (the constant of proportionality obtained by the fit is close to unity, namely 0.97). Thus, an increase of peak growth rates yields an even stronger increase of the consumption speed enhancement factor.

To assess the effect of the different flame parameters such as the Zeldovich number β, the expansion ratio σ, and the effective Lewis number Le_{eff} on the peak growth rate ω_{max}, it is important to note that β, σ, and Le_{eff} change simultaneously during some of the parametric variations, e.g. during the variation of equivalence ratio. Thus, to assess the effect of the different flame parameters on the consumption speed enhancement $s_{\text{c}}/s_{\text{L}}$, the following joint scaling law, similar to the one employed for the linear growth rates in part 1 of this work [1], is used.

$$\frac{\left(\frac{s_{\text{c}}}{s_{\text{L}}}\right) - 1}{\left(\frac{s_{\text{c}}}{s_{\text{L}}}\right)_{\text{Ref}} - 1} = \left(\frac{\sigma}{\sigma_{\text{Ref}}}\right)^{\gamma_\sigma} \left(\frac{\beta}{\beta_{\text{Ref}}}\right)^{\gamma_\beta} \left(\frac{Le_{\text{eff}}}{Le_{\text{eff,Ref}}}\right)^{\gamma_{Le_{\text{eff}}}}, \tag{21}$$

where the reference values of s_{c}, σ, β, and Le_{eff} are taken from case 'Ref'. Note that Eq. 21 is not derived from first principles, but represents one way among other possible options to efficiently disentangle the effect of the different parameters on the consumption speed enhancement. Similar power law fits have been suggested, e.g. to assess the critical radius, which characterizes the onset of intrinsic instabilities in spherically expanding flames [34], to assess the variability of the cut-off wave length with pressure [35], or generally, for flame parameters such as the laminar burning velocity [36]. In the following, the suitability of assessing $s_{\text{c}}/s_{\text{L}}$ by Eq. 21 is discussed. For this, the three scaling coefficients γ_{i} are fitted to the values of

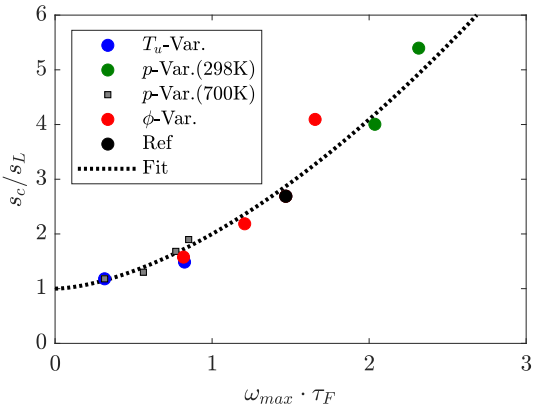

Figure 16: Comparison of the numerically measured peak growth rates in the linear regime (abscissa) versus the increase of consumption speed $s_{\text{c}}/s_{\text{L}}$ in the non-linear regime (ordinate) for all cases. The dotted lines is the fit of Eq. 20 to the data points yielding $\zeta = 1.63$

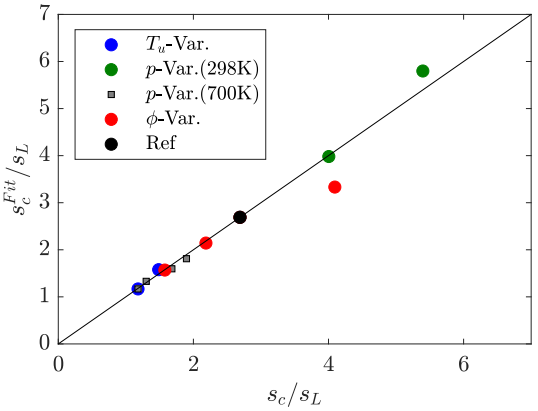

Figure 17: Power law based on $[\sigma, \beta, Le_{\text{eff}}]$: Comparison of the numerically measured increase of consumption speed $s_{\text{c}}/s_{\text{L}}$ (abscissa) versus the predicted values by Eq. 21 (ordinate).

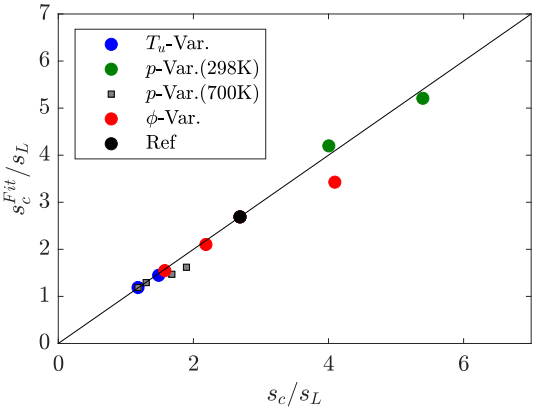

Figure 18: Power law based on $[\phi, T_{\text{u}}, p]$: Comparison of the numerically measured increase of consumption speed $s_{\text{c}}/s_{\text{L}}$ (abscissa) versus the predicted values by Eq. 23 (ordinate).

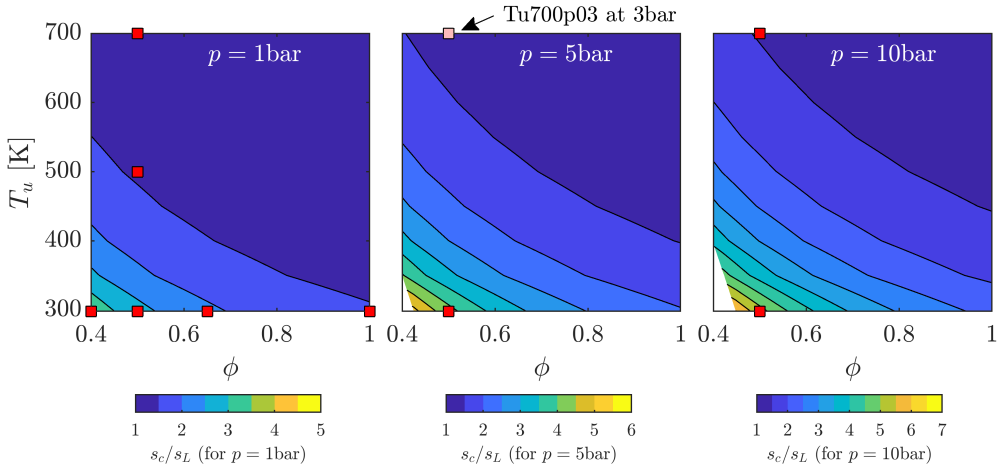

Figure 19: Variation of the consumption speed enhancement factor s_c/s_L for different values of equivalence ratio ϕ, unburned temperature T_u, and pressure p; visualized by means of Eq. 23 and red squares represent simulations. Note that case 'Tu700p03' has been only schematically inserted into the panel at p = 5bar (light red color) as its pressure value is p = 3bar.

σ, β, Le_{eff}, and s_c/s_L of the different cases. The data from cases 'Tu700p03', 'Tu700p10', and 'Tu700p20' are not used to fit the coefficients γ_i but used for an assessment of the quality of the fit.

Fig. 17 shows a comparison of the actual values of s_c/s_L and the values predicted by Eq. 21. It is worth noting that case 'Tu700' is displayed twice (blue dot that contains a grey box) as it belongs to the parametric variations of unburned temperature and pressure at elevated temperatures. Generally, good agreement among the actual and predicted values is observed and even for the parametric variation of pressure at elevated unburned temperatures (grey boxes) that has not been used for the fit, good agreement is achieved by Eq. 21. As only the Zeldovich number β changes during the pressure variation at elevated unburned temperatures, this indicates a robust fit with respect to the Zeldovich number β. The least squares fit yields for the exponents the values

$$\gamma_\sigma = 1.03, \quad \gamma_\beta = 1.57, \quad \gamma_{Le_{\text{eff}}} = -1.36. \tag{22}$$

Similar to the peak growth rates, an increase of the expansion ratio σ and Zeldovich number β and a decrease of the effective Lewis number Le_{eff} yield an increase of the consumption speed enhancement due to an increasing impact of the intrinsic flame instabilities.

For the sake of completeness, a similar analysis can be performed to assess the effect of equivalence ratio, unburned temperature, and pressure on the consumption speed enhancement. For this, the following power law is proposed

$$\frac{\left(\frac{s_c}{s_L}\right) - 1}{\left(\frac{s_c}{s_L}\right)_{\text{Ref}} - 1} = \left(\frac{\phi}{\phi_{\text{Ref}}}\right)^{\gamma_\phi} \left(\frac{T_u}{T_{u,\text{Ref}}}\right)^{\gamma_{T_u}} \left(\frac{p}{p_{\text{Ref}}}\right)^{\gamma_p} \tag{23}$$

Similarly to Eq. 21, this power law aims to quantify the scaling of the consumption speed enhancement with respect to ϕ, T_u, p. The three scaling coefficients γ_i are fitted to the values of ϕ, T_u, p, and s_c/s_L of the different cases and the data from cases 'Tu700p03', 'Tu700p10', and 'Tu700p20' are not used to fit the coefficients γ_i but used for an assessment of the quality of the fit. It is worth noting that in Eqs. 21 and 23, case 'Ref' has been used for evaluating the coefficients in the denominator. While choosing a different case or using instead a power law that uses a constant of proportionality, which replaces the coefficients labeled with the index 'Ref' and is fitted together with the exponents γ_i, could affect the values of the exponents γ_i, it is shown in the supplementary material that such variations do not significant affect the determination of the exponents γ_i. The comparison among predicted and actual values of s_c/s_L for Eq. 23 is provided in Fig. 18. Good agreement between predicted and measured values is found for the parametric variations at ambient conditions while the values of s_c/s_L of the parametric variation at elevated temperatures show a slightly different trend towards higher pressures indicating some uncertainty with respect to the pressure scaling. The following values γ_i are obtained

$$\gamma_\phi = -1.62, \quad \gamma_{T_u} = -2.56, \quad \gamma_p = 0.40. \tag{24}$$

While the exponents γ_ϕ, γ_{T_u}, and γ_p suggest a significantly stronger effect of variations of the unburned temperature on the consumption speed enhancement than pressure, it is important to also consider the typical range of variations of these parameters in relevant applications, e.g. the term p/p_{Ref} may be large while the variations of the unburned temperature expressed by the term $T_u/T_{u,\text{Ref}}$ are typically moderate. Therefore, Fig. 19 shows the value of s_c/s_L that is determined from the power law according to Eq. 23 for different values of ϕ and T_u at three distinct values of pressure. The different cases are marked by red squares and case 'Tu700p03' has been only schematically inserted into the panel at p = 5bar (light red color), while its pressure value is p = 3bar, to indicate that simulation data also exist for intermediate pressure values at elevated temperatures. Further, for lean conditions, the parametric variation is confined by the lean flammability limit, which here, is defined by an un-

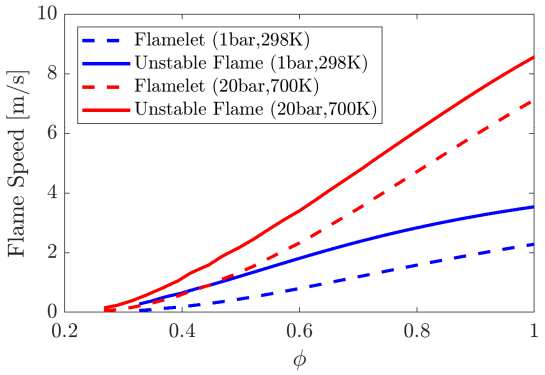

Figure 20: Comparison of the variation of the consumption speed s_c (solid lines) predicted by Eq. 23 and the unstretched laminar burning velocity s_L (dashed lines) with respect to equivalence ratio at ambient conditions and at elevated pressure and temperature.

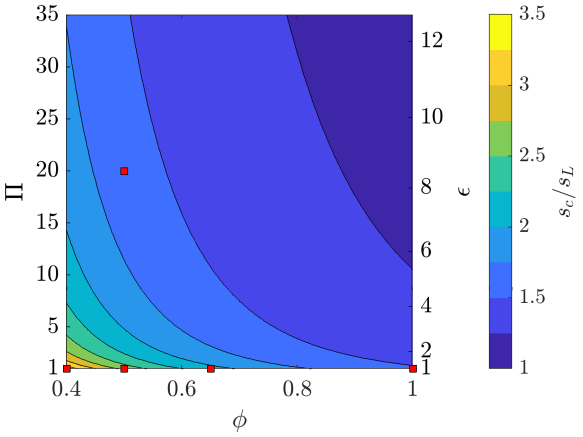

Figure 21: Variation of the consumption speed enhancement factor s_c/s_L for different pressure ratios Π and equivalence ratios ϕ if assuming an isentropic compression prior to combustion that starts at $p_0 = 1$ bar and $T_{u,0} = 298$ K.. For reference, the compression ratio is indicated on the right ordinate and the cases of the equivalence ratio variation and case 'Tu700p20' are displayed as red squares.

stretched laminar flame speed s_L that is smaller than 5 cm/s, so no values of s_c/s_L are visible in the bottom left corner of the two right panels. Generally, an increase of s_c/s_L towards leaner conditions and lower unburned temperatures and an increase of s_c/s_L with increasing pressure can be seen. While an increase of unburned temperature is seen to significantly reduce the consumption speed enhancement and, hence, intrinsic instabilities, pressure is seen to also have a significant effect on s_c/s_L as significantly larger values are obtained in the right panel at $p = 10$bar. Finally, note that towards the lean flammability limit at higher pressures, a large enhancement of s_c/s_L is seen. While this is qualitatively expected, it is important to stress that these values represent a certain extrapolation of Eq. 23 with respect to the performed simulations and may require further analysis and validation. Further note that very similar trends are observed if using Eq. 21 for Fig. 19 as shown in the supplementary material.

While the ratio s_c/s_L increases towards unstable conditions according to Fig. 19, the unstretched laminar burning velocity s_L of a planar flame is also decreasing simultaneously. For instance, Fig. 20 shows a comparison of the (unnormalized) consumption speed s_c and the unstretched laminar burning velocity s_L for the parametric variation of equivalence ratio at ambient conditions (blue lines) and at elevated pressure and temperature (red lines). Even though the consumption speed s_c is significantly higher than s_L, still a decrease of flame speeds towards leaner mixtures is visible as the increase of s_c/s_L does not compensate the reduction of s_L towards leaner mixtures.

Finally, in typical combustion devices, the temperature and pressure prior to the combustion process are coupled due to the preceding compression, e.g. in compression engines or gas turbines. Therefore, Fig. 21 shows the enhancement factor of consumption speed s_c/s_L for different pressure ratios $\Pi = p/p_0$ and equivalence ratios ϕ, while the unburned temperature is assumed to follow an isentropic compression as

$$T_u = T_{u,0} \cdot \Pi^{(\hat{\gamma}-1)/\hat{\gamma}} \tag{25}$$

The heat capacity ratio $\hat{\gamma}$ is assumed as $\hat{\gamma} = 1.4$ and ambient conditions are picked for the reference values with $p_0 = 1$ bar and $T_{u,0} = 298$ K. Additionally, Fig. 21 displays the compression ratio $\epsilon = v_0/v$, which is the ratio of the specific volumes v and v_0 after and prior to compression. The compression ratio is linked to the pressure ratio by $\epsilon = \Pi^{(1/\hat{\gamma})}$. The values of s_c/s_L are determined from the correlation in Eq. 23 and in addition, the cases of the equivalence ratio variation and case 'Tu700p20' are displayed (red squares) in Fig. 21 (the pressure and unburned temperature of the other cases do not follow Eq. 25, so they are not shown). While the effect of unburned temperature is seen to compensate the effect of pressure as s_c/s_L is decreasing for larger values of Π or ϵ, respectively, also a significant increase of s_c/s_L towards leaner mixtures is observed, which resemble part load conditions, e.g. in hydrogen compression engines. Thus, even though some values of s_c/s_L may require further validation at very lean conditions as they represent an extrapolation with respect to the considered simulations, this still indicates that intrinsic instabilities may not be neglected at such conditions.

5. Conclusions

The propensity of lean premixed hydrogen flames to develop intrinsic instabilities is studied by means of a series of simulations at different equivalence ratios, unburned temperatures, and pressures. The propagation of all flames is subject to the hydrodynamic and thermodiffusive instability mechanism whose impact on the flame propagation varies among the different cases. In this part of this work, the long-term dynamics of these flames are studied, while in part 1 of this work, only the initial phase of weakly perturbed planar flames at the same conditions has been analyzed.

For low equivalence ratios, low unburned temperatures, and for high pressures, an increasing impact of intrinsic instabilities on the flame dynamics is observed yielding strongly corrugated flames with significant variations of the local reaction rates and

local extinction. These trends are consistent with the stability analysis in part 1 of this work, where increasing growth rates of the dispersion relations are observed for unstable conditions. The fluctuations of the reaction rates are linked to fluctuations of the local equivalence ratio or mixture fraction, respectively, that arise from the differential diffusion of hydrogen. Hence, a joint description of mixture fraction and progress variable is required to adequately analyze the flame state. Furthermore, intrinsic instabilities lead to a significant enhancement of the consumption speed relative to the laminar unstretched burning velocity due to an increase of flame surface area and flame reactivity. While both surface area and flame reactivity increase if equivalence ratio and unburned temperature are reduced, the increase of pressure mainly leads to an increase of flame reactivity and does not significantly enhance flame wrinkling. The increase of reactivity is also found to correspond to a significant deviation of the flame displacement speed with respect to the value obtained from an unstretched laminar flamelet.

The maximum growth rates of the dispersion relations, which were obtained from a stability analysis conducted in part 1 of this work, are found to correlate well with the consumption speed enhancement. Consistent with the analysis of the growth rates, an increase of the expansion ratio or the Zeldovich number, or a decrease of the effective Lewis number lead to an increasing flame speed enhancement. Considering typical combustion devices that undergo an isentropic compression prior to combustion, a reduction of instabilities towards higher pressure ratios or compression ratios, respectively, is observed indicating that the enhancement of instabilities due to an increase of pressure is over compensated by the opposite effect of increasing unburned temperatures.

Finally, it is worth mentioning that the performed analyses are restricted to two-dimensional flows and do not consider effects due to three-dimensional flame front corrugations or the interaction of instabilities with turbulent flows, which require further analyses in future work.

Acknowledgment

Generous support of the Deutsche Forschungsgemeinschaft (DFG) under grant number PI 368/9-1 is gratefully acknowledged. Computational resources have been provided by the Gauss Centre for Supercomputing e.V. on the GCS Supercomputer SuperMuc at Leibniz Supercomputing Centre in Munich.

References

[1] L. Berger, A. Attili, H. Pitsch, Enhancement of Intrinsic Instabilities in Premixed Hydrogen Flames due to Variations of Pressure, Equivalence Ratio, and Temperature: Part 1 - A Stability Analysis of Planar Flames, Combust. Flame (2021).

[2] S. Kadowaki, H. Suzuki, H. Kobayashi, The unstable behavior of cellular premixed flames induced by intrinsic instability, Proc. Comb. Inst. 30 (2005) 169–176.

[3] S. Kadowaki, T. Hasegawa, Numerical simulation of dynamics of premixed flames: flame instability and vortex–flame interaction, Prog. Energ. Combust. 31 (2005) 193–241.

[4] J. Yuan, Y. Ju, C. K. Law, On flame-front instability at elevated pressures, Proc. Comb. Inst. 31 (2007) 1267–1274.

[5] G.J. Sharpe, S.A.E.G. Falle, Nonlinear cellular instabilities of planar premixed flames: numerical simulations of the Reactive Navier–Stokes equations, Combust. Theor. Model. 10 (2006) 483–514.

[6] C. Altantzis, C. E. Frouzakis, A. G. Tomboulides, M. Matalon, K. Boulouchos, Hydrodynamic and thermodiffusive instability effects on the evolution of laminar planar lean premixed hydrogen flames, J. Fluid Mech. 700 (2012) 329–361.

[7] C. Altantzis, C. E. Frouzakis, A. G. Tomboulides, S. G. Kerkemeier, K. Boulouchos, Detailed numerical simulations of intrinsically unstable two-dimensional planar lean premixed hydrogen/air flames, Proc. Comb. Inst. 33 (2011) 1261–1268.

[8] C.E. Frouzakis, N. Fogla, A.G. Tomboulides, C. Altantzis, M. Matalon, Numerical study of unstable hydrogen/air flames: Shape and propagation speed, Proc. Combust. Inst. 35 (2015) 1087–1095.

[9] J.F. Yu, R. Yu, X.S. Bai, M.B. Sun, J.G. Tan, Nonlinear evolution of 2D cellular lean hydrogen/air premixed flames with varying initial perturbations in the elevated pressure environment, Int. J. Hydrogen Energ. 42 (2017) 3790–3803.

[10] D. Fernández-Galisteo, V.N. Kurdyumov, P.D. Ronney, Analysis of premixed flame propagation between two closely-spaced parallel plates, Combust. Flame 190 (2018) 133–145.

[11] L. Berger, K. Kleinheinz, A. Attili, H. Pitsch, Characteristic patterns of thermodiffusively unstable premixed lean hydrogen flames, Proc. Comb. Inst. 37 (2019) 1879–1886.

[12] J. Wongwiwat, J. Gross, P.D. Ronney, Flame Propagation in Narrow Channels at Varying Lewis Number, 25th International Colloquium on the Dynamics of Explosions and Reactive Systems (2015).

[13] D. Bradley, C.G. W. Sheppard, R. Woolley, D.A. Greenhalgh, R.D. Lockett, The Development and Structure of Flame Instabilities and Cellularity at Low Markstein Numbers in Explosions, Combust. Flame 122 (2000) 195–209.

[14] R.J.M. Bastiaans, A.W. Vreman, H.Pitsch, DNS of lean hydrogen combustion with flamelet-generated manifolds, CTR Annual Res. Briefs (2007) 195–206.

[15] J.D. Regele, E. Knudsen, H. Pitsch, G. Blanquart, A two-equation model for non-unity Lewis number differential diffusion in lean premixed laminar flames, Combust. Flame 160 (2013) 240–250.

[16] J.A. van Oijen, A. Donini, R.J.M. Bastiaans, J.H.M. ten Thije Boonkkamp, L.P.H. de Goey, State-of-the-art in premixed combustion modeling using flamelet generated manifolds, Prog. Energy Combust. Sci. 57 (2016) 30–74.

[17] R. Bastiaans, A.W. Vreman, Numerical simulation of instabilities in lean premixed hydrogen combustion, Int. J. Numer. Method. H. 22 (2012) 112–128.

[18] H. Boughanem, A. Trouvé, The domain of influence of flame instabilities in turbulent premixed combustion, Proc. Comb. Inst. 27 (1998) 971–978.

[19] V. Bychkov, Importance of the Darrieus-Landau instability for strongly corrugated turbulent flames, Phys. Rev. E 68 (2003).

[20] A.J. Aspden, M.S. Day, J.B. Bell, Turbulence-chemistry interaction in lean premixed hydrogen combustion, Proc. Comb. Inst. 35 (2015) 1321–1329.

[21] P. Chiesa, G. Lozza, L. Mazzocchi, Using hydrogen as gas turbine fuel, J. Eng. Gas Turb. Power 127 (2005) 73–80.

[22] F. Creta, P.E. Lapenna, R. Lamioni, N. Folga, M. Matalon, Propagation of premixed flames in the presence of Darrieus–Landau and thermal diffusive instabilities, Combust. Flame 216 (2020) 256–270.

[23] A. Tomboulides, J. Lee, S. Orszag, Numerical simulation of low Mach number reactive flows, J. Scientif. Comput. 12 (1997) 139–167.

[24] M.P. Burke, M. Chaos, Y. Ju, F.L. Dryer, S.J. Klippenstein, Comprehensive H_2/O_2 kinetic model for high-pressure combustion, Int. J. Chem. Kinet. 44 (2012) 444–474.

[25] H. Pitsch, A C++ program package for 0D combustion and 1D laminar flames, 1998.

[26] A. Moreau, O. Teytaud, J. P. Bertoglio, Optimal estimation for large-eddy simulation of turbulence and application to the analysis of subgrid models, Phys. Fluids 18 (2006).

[27] L. Berger, K. Kleinheinz, A. Attili, F. Bisetti, H. Pitsch, M.E. Mueller, Numerically accurate computational techniques for optimal estimator analyses of multi-parameter models, Combust. Theor. Model. 22 (2018) 480–504.

[28] T. Poinsot, D. Veynante, Theoretical and numerical combustion, Edwards,

2005.

[29] R.W. Bilger, S.H. Starner, R.J. Kee, On reduced mechanisms for methane-air combustion in nonpremixed flames, Combust. Flame 80 (1990) 135–149.

[30] A.Y. Klimenko, A.G. Class, Propagation of non-stationary curved and stretched premixed flames with multi-step reaction mechanisms, Combust. Sci. Technol. 174 (2002) 165–207.

[31] G.K. Giannakopoulos, A. Gatzoulis, C.E. Frouzakis, M. Matalon, A.G. Tomboulides, Consistent definitions of "flame displacement speed" and "Markstein length" of premixed flame propagation, Combust. Flame 162 (2015) 1249–1264.

[32] L. Vervisch, E. Bidaux, K.N.C. Bray, W. Kollmann, Surface density function in premixed turbulent combustion modeling, similarities between probability density function and flame surface approaches, Phys. Fluids 7 (1995) 2496–2503.

[33] A. Attili, S. Luca, D. Denker, F. Bisetti, H. Pitsch, Turbulent flame speed and reaction layer thickening in premixed jet flames at constant Karlovitz and increasing Reynolds numbers, Proc. Comb. Inst. (2020).

[34] J. Beeckmann, R. Hesse, S. Kruse, A. Berens, N. Peters, H. Pitsch, M. Matalon, Propagation speed and stability of spherically expanding hydrogen/air flames: Experimental study and asymptotics, Proc. Comb. Inst. 36 (2017) 1531–1538.

[35] A. Attili, R. Lamioni, L. Berger, K. Kleinheinz, P.E. Lapenna, H. Pitsch, F. Creta, The effect of pressure on the hydrodynamic stability limit of premixed flames, Proc. Comb. Inst. 38 (2021) 1973–1981.

[36] Y. Wang, A. Movaghar, Z. Wang, Z. Liu, W. Sun, F.N. Egolfopoulos, Z. Chen, Laminar flame speeds of methane/air mixtures at engine conditions: Performance of different kinetic models and power-law correlations, Combust. Flame 218 (2020) 101–108.